Please cite this article in press as: Cao et al., Lithium Dendrite in All-Solid-State Batteries: Growth Mechanisms, Suppression Strategies, and Characterizations, Matter (2020), https://doi.org/10.1016/j.matt.2020.03.015

Matter

CellPress
REVIEWS

Review

Lithium Dendrite in All-Solid-State Batteries: Growth Mechanisms, Suppression Strategies, and Characterizations

Daxian Cao,[1] Xiao Sun,[1] Qiang Li,[1] Avi Natan,[1] Pengyang Xiang,[1] and Hongli Zhu[1,*]

Li metal has been attracting increasing attention as an anode in all-solid-state batteries because of its lowest electrochemical potential and high capacity, although the problems caused by dendritic growth impedes its further application. For a long time, all-solid-state Li metal batteries (ASLBs) are regarded to revive Li metal due to high mechanical strength. However, numerous works revealed that the dendrite issue widely exists in ASLBs, and the mechanism is complex. This review provides a systematic and in-depth understanding of the thermodynamic, kinetic, electrochemical, chemomechnical, structural stability, and characterizations of Li dendrite in ASLBs. First, the mechanisms for dendrite formation and propagation in polymer, ceramic and glass electrolyte were discussed. Subsequently, based on these mechanisms of dendrite growth, we reviewed various strategies for dendrite suppression. Furthermore, advanced characterization techniques were reviewed for better understanding of dendrite in solid-state batteries.

INTRODUCTION

Given the continually accelerating demand in modern society, energy-storage systems with high energy and power density have never been more crucial.[1,2] Among various candidates, lithium-ion batteries (LIBs) are one of the most successfully and pervasively applied technologies to meet this need.[3,4] Since first being commercialized in 1991, the state-of-the-art LIBs have reached the upper limit in energy density, 256 Wh kg^{-1} at cell level.[5] To compete with the combustion engines in automobiles that have an energy density higher than 1000 Wh kg^{-1}, the energy density for LIBs needs to be improved for fully electric vehicles (EVs).[6] The other issue with the traditional LIBs is the employment of flammable organic liquid electrolytes (OLEs), which poses severe safety concern of catching fire and explosions.

Considering the aforementioned limitations of LIBs, all-solid-state Li metal batteries (ASLBs) that replace OLEs with solid-state electrolytes (SEs) have been extensively pursued as next-generation rechargeable batteries. SEs are safer than the flammable organic solvents used in conventional LIBs, since most SEs are made of ceramics, glass, and/or their composites, all of which are non-flammable or feature outstanding high-temperature stability. Hence, ASLBs can eliminate risks such as fire and explosion. More importantly, SEs are commonly considered as a reliable electrolyte to concurrently match high-energy density cathode and Li metal anode, enabling next-generation high-energy batteries such as Li-sulfur and Li-oxygen batteries. Applying Li metal as the anode is critical to meet the requirements of EVs because Li metal has an ultra-high specific capacity (3,860 mAh g^{-1} in theory) and the lowest electrochemical potential (−3.04 V versus standard hydrogen electrode).[7] Although the study of Li metal anode predates the birth of conventional

Progress and Potential

Driven by the increasing demand for energy worldwide, the development of high-energy, high-power, safe, and reliable batteries is one of the most important goals at the forefront of energy research. Li metal has been receiving increasing attention as an anode in all-solid-state-batteries (ASLBs) because of its lowest electrochemical potential, high capacity, and light weight. However, Li metal application is highly impeded by the problematic dendrite issue. For a long time, ASLBs were regarded to revive Li metal due to high mechanical strength. However, recent studies have proved that the Li dendrite also grows and propagates in the solid electrolyte during cycling, and even more severely than in batteries using liquid electrolytes, because of the uneven charge distribution at the interface of electrolyte and electrode. Many efforts have been devoted to study Li metal dendrite in liquid electrolyte. Still, as of yet there is no comprehensive in-depth review to summarize the mechanisms and corresponding suppression strategies of dendrite in ASLBs. In this review, a systematic discussion of dendrite growth mechanisms, the

LIBs, the severe dendrite growth in OLEs accompanied with rapidly decaying performance and safety issues caused by short circuit have inhibited its commercialization. In OLEs, dendrite growth is rooted in the inhomogeneous deposition and dissolution of Li metal, which is related to the formation of an unstable solid electrolyte interphase (SEI) between Li metal and electrolyte. To address this problem, various modifications of electrolyte, Li metal anode, and separator have been reported, for example, employment of superconcentrated electrolyte,[8] introducing additives to the electrolyte,[9] forming artificial SEI,[10] and fabricating structured Li metal.[11]

For a long time, SEs were thought as a potential solution of the dendrite issue because of their high mechanical strength. According to the widely cited Monroe and Newman model, dendrite growth can be successfully suppressed if the shear modulus of SEs is 2-fold larger than that of Li (4.8 GPa at 298 K).[12] Several SEs are reported to possess relatively high elastic modulus,[13] such as garnet-type $Li_7La_3Zr_2O_{12}$ (LLZO) with an extremely high shear modulus of ~100 GPa,[14] 80% dense bulk β-Li_3PS_4 with bulk modulus of 10–12 GPa,[15] and even some polymer electrolytes with mechanical strength of 12 GPa.[16] However, recent reports have found that the Li dendrite can still form and propagate in these high-strength SE-based cells during cycling under limited current densities.[17] The critical current density (CCD), i.e., the largest current density allowed without shorting, is usually reported as lower than 1 mA cm^{-2} in ASLBs. Furthermore, the short circuit occurring in ASLBs is even faster than that in batteries using OLEs, which is beyond expectation. It has been also reported that polymer electrolyte with shear modulus of the same order of magnitude as Li could suppress dendrite growth and thereby increase lifetime and safety.[18] This suggests that mechanical strength is not the only factor that affects dendrites. Considering inherently different chemical and physical conditions in OLEs, the mechanism of dendrite growth in SEs is much more complex and miscellaneous. Much effort using both theory and experiments has been devoted to understand such mechanisms, but an in-depth and comprehensive review to summarize the mechanisms and corresponding suppression strategies is still lacking. Even though some excellent reviews on the unstable interface between the SEs and Li, and the failure mechanisms of ASLBs have been published, the dendrite issue has been just briefly discussed.[19–21] Considering the significant progress that has been made recently in the investigation of the failure mechanism of Li metal in ASLBs, this review thus represents a timely and important overview of recent advances.

In this review, for the first time the potential mechanisms of dendrite growth in ASLBs, the corresponding Li dendrite suppression strategies, and several advanced characterization techniques are systematically discussed and summarized. First, based on a common classification of SEs, the review begins with the mechanism of dendrite growth in solid polymer electrolytes (SPEs) and solid ceramic or glass electrolytes (SCEs). Thereafter, based on these primary mechanisms, various strategies for addressing the dendrite issue are discussed. Polymer-based composites, optimization of Li and SEs, the formation of the metastable interlayer, and the introduction of an artificial interface layer are underscored. Finally, multiple advanced characterization techniques for the investigation of dendrite growth in SEs are discussed.

corresponding Li dendrite suppression strategies, and advanced characterization techniques in ASLBs are critically discussed and summarized.

DENDRITE GROWTH MECHANISMS

Currently, SEs are classified into organic polymer electrolytes, inorganic ceramic or glass electrolytes, and their composites.[22] The composites are generally utilized to

[1]Department of Mechanical and Industrial Engineering, Northeastern University, 360 Huntington Avenue, Boston, MA 02115, USA

*Correspondence: h.zhu@neu.edu

https://doi.org/10.1016/j.matt.2020.03.015

Please cite this article in press as: Cao et al., Lithium Dendrite in All-Solid-State Batteries: Growth Mechanisms, Suppression Strategies, and Characterizations, Matter (2020), https://doi.org/10.1016/j.matt.2020.03.015

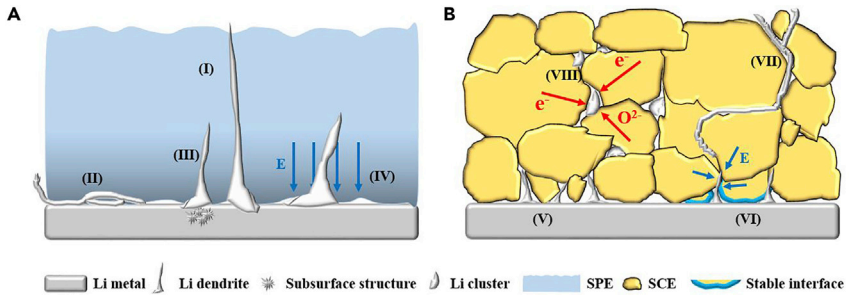

Figure 1. Dendrite Growth Mechanisms in Solid-State Electrolytes.
Schematic illustrating the dendrite growth mechanism in organic solid polymer electrolyte (A) and inorganic ceramic/glass electrolyte (B).

combine the benefits of polymer and ceramic materials. Due to the inherent differences between SCEs and SPEs, it is necessary to discuss the dendrite growth mechanism separately.

The possible mechanisms for dendrite nucleation in relation to their dendrites in SPEs and SCEs are schematically illustrated in Figures 1A and 1B, respectively. To gain a better understanding, we summarize and classify them into scenarios whose details will be discussed in the relevant subsections.

In the section Organic Solid Polymer Electrolyte:
Scenario I. Dendrite grows at the tip and penetrates the SPE through the soft part. (Dendrite Growth at the Tip)
Scenario II. Dendrite grows laterally and extends from the side of electrode and SPE. (Lateral Growth of Dendrite)
Scenario III. Subsurface structure buried under dendritic structure triggers the formation of dendrite. (Subsurface Structure Triggers Dendrite Growth)
Scenario IV. Additional effect caused by the redistribution of charge in Li|SPE interface induces Li dendrite. (Redistributed Charges at Li|SE Interface Accelerate Dendrite Formation)
In the section Inorganic Solid Ceramic/Glass Electrolyte:
Scenario V. Physical issues, such as the microstructure on the surface, void and defect within, and density of the SCE cause dendrite nucleation and growth. (Discontinuous Interface Contact-Induced Dendrite Growth)
Scenario VI. Grain boundaries induce Li propagation inside the SCE. (Grain Boundary-Induced Li Dendrite Penetration)
Scenario VII. Electrons from the residual conductivity, oxygen framework, and pore surface induce the formation of Li cluster inside the SCE. (Li Plating Inside Solid Ceramic or Glass Electrolyte)
Scenario VIII. Enhanced electric field at the tips due to the highly stable chemical interface between SCE and Li triggers dendrite growth. (Interphase Effect on Dendrite Growth)

Organic Solid Polymer Electrolyte

The formation of Li dendrites in cells results from Li nucleation and growth, which are greatly affected by the electrolyte. The soft nature of the SPEs is regarded as the prime reason for dendrite penetration, although it grants good flexibility and high processability. The sharp dendrite easily grows in the SPEs and eventually causes short circuit of the battery. Various factors are summarized below to explain the

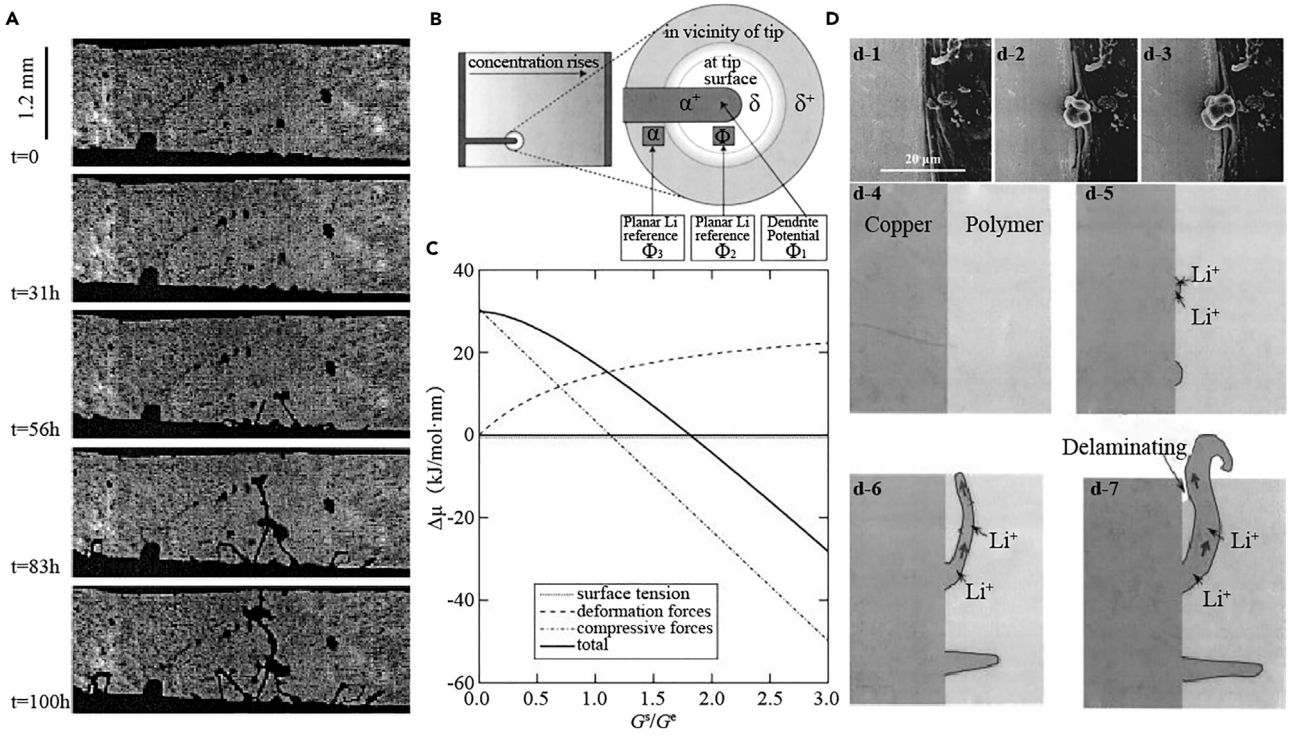

Figure 2. Dendrite Growth at the Tip or in Lateral

(A) The penetration of Li dendrite in polymer electrolyte. Adapted with permission from Brissot et al.[24] Copyright 1999, Elsevier Inc.

(B) Diagram of the region near the dendrite tip to show how dendrite grows at the tip. Adapted with permission from Monroe and Newman.[25] Copyright 2003, IOP Publishing Ltd.

(C) Contributions of surface tension, deformation forces, and compressive forces to the interfacial stability parameter as a function of SE shear modulus. Adapted with permission from Monroe and Newman.[12] Copyright 2005, IOP Publishing Ltd.

(D) Li dendrite growth in lateral and extension from the side of Cu and SPE as a function of time: before (d-1), after 160 min (d-2), and after 200 min (d-3). (d-4 to d-7) Schematic illustration of the mechanism of dendrite growth in the side. Adapted with permission from Dolle et al.[17] Copyright 2002, IOP Publishing Ltd.

dendrite issue in SPEs: dendrite growth at the tip or laterally, subsurface structure-induced nucleation, and redistribution of charges at the Li|SPE interface that accelerating dendrite growth.

Dendrite Growth at the Tip

Tip deposition is usually used to explain dendritic growth. The protrusions at the surface of the electrode generate enhanced electric and ionic fields near the spherical tip, which strongly affect the deposition behavior.[23] In 1999, Brissot and colleagues *in situ* observed the dendrite growth in a symmetric Li|polymer|Li cell.[24] Needle-like dendrites gradually grew at the tip as the electrodeposition time increased and eventually pierced the poly(ethylene oxide) (PEO)-based electrolyte (Figure 2A). They found that ionic concentration in the electrolyte around the dendrites significantly affected dendrite growth. Monroe and Newman built a surface-energy-controlled and tip-curvature-affected model in a parallel electrode Li|polymer|Li cell to explain the dendritic growth of Li in SPE (Figure 2B).[25] According to their theory, Li deposition was more likely to happen at the dendrite tip, due to the relatively faster accumulation of electric charges than in the smooth region. The dendrite grows and penetrates through the polymer once activated, although lowering the current density and enlarging the distance between electrodes that could slow the growth rate. With a linear elasticity theory, Monroe

Please cite this article in press as: Cao et al., Lithium Dendrite in All-Solid-State Batteries: Growth Mechanisms, Suppression Strategies, and Characterizations, Matter (2020), https://doi.org/10.1016/j.matt.2020.03.015

and Newman investigated the impact of elastic deformation on the Li deposition kinetics.[12] According to their theory, surface tension force, deformational force across the interface, and compressive force contributed to the interface stability together. As shown in Figure 2C, in contrast to deformational force, it is the compressive force that contributes most to the interface stability. A stable interface will be formed if the shear moduli of separator, i.e., SPE, has the same order of modulus of Li, and the dendrite could be mechanically suppressed when the shear modulus of SPE is about twice that of Li.

Lateral Growth of Dendrite

Supplementing the widely held tip-induced dendrite growth, Dolle et al. found that the dendrite could also propagate laterally, observed from live scanning electron microscopy (SEM) (Figure 2D).[17] In a copper|polymer|copper system, as the deposition occurred, the dendrite kept growing even after the tip was out of the electrolyte. They concluded that the Li ions deposit through the SEI laterally and thus accelerate dendrite growth. As a result, the lateral growth of Li dendrite led to delamination between the electrode and polymer electrolyte. The insufficient contact between SPE and electrode was also believed to induce dendrite protrusion due to the free space formed for dendrite growth.[19]

Subsurface Structure-Triggered Dendrite Growth

Most investigations of dendrite growth focused on the deposition of Li at the SE|Li interface, but overlooked the subsurface structure of dendrite before it protruded from the electrode. Using synchrotron hard X-ray microtomography, Harry et al. analyzed the Li|polymer interface at the early stage of dendrite development.[26] As shown in Figure 3A, the bulk of dendrite appeared beneath the interface before it protruded into the polymer electrolyte. In the beginning, dendritic structure was not observed whereas, as the deposition proceeded, subsurface structure appeared and its volume was significantly larger than the tip in the polymer. Eventually, the dendrite penetrated the solid-state polymer electrolyte. The burgeoning growth process of dendrites was depicted in three-dimensional (3D) reconstructed volumes, which clearly revealed that most dendrites were buried under the electrode but did not reside within the electrolyte in the early stage of dendrite development. Compared with dendrite growth in polymer electrolyte at the tip and side, the subsurface structure greatly affected dendrite nucleation in the initial process.

Redistributed Charges at Li|SE Interface Accelerates Dendrite Formation

The additional phenomenon caused by redistribution of charges at the Li|SE interface also affected the Li deposition.[29] Representative works have confirmed the existence of a space charge layer during the electrochemical deposition process and the direct consequence of the ramified growth.[30,31] In ASLBs, due to the redistribution of Li^+ ions rendered by the difference in chemical potential of Li^+ between electrode and electrolyte, the space charge layer widely exists at the interface between the SE, cathode, and anode, which causes detrimental interfacial impedance.[32,33] The space charge layer in the cathode|SE side has been well studied, while the study of that at the Li|SE interface is still scarce. Zhou et al. have found that the redistribution of charges significantly affects dendrite nucleation (Figure 3B).[27] Suffering from the relatively low Li^+ transfer number, the rapid anion depletion in PEO-based electrolyte produced a double-layer electric field across the Li|polymer interface during changing, which enhanced the Li deposition and accelerated the decomposition of electrolyte and nucleation of dendrites. As a result, the interface impedance increased dramatically, indicating the unstable interface. The intrinsic low Li^+ transfer number was the drawback of most organic polymer electrolytes.[34] Cao et al.

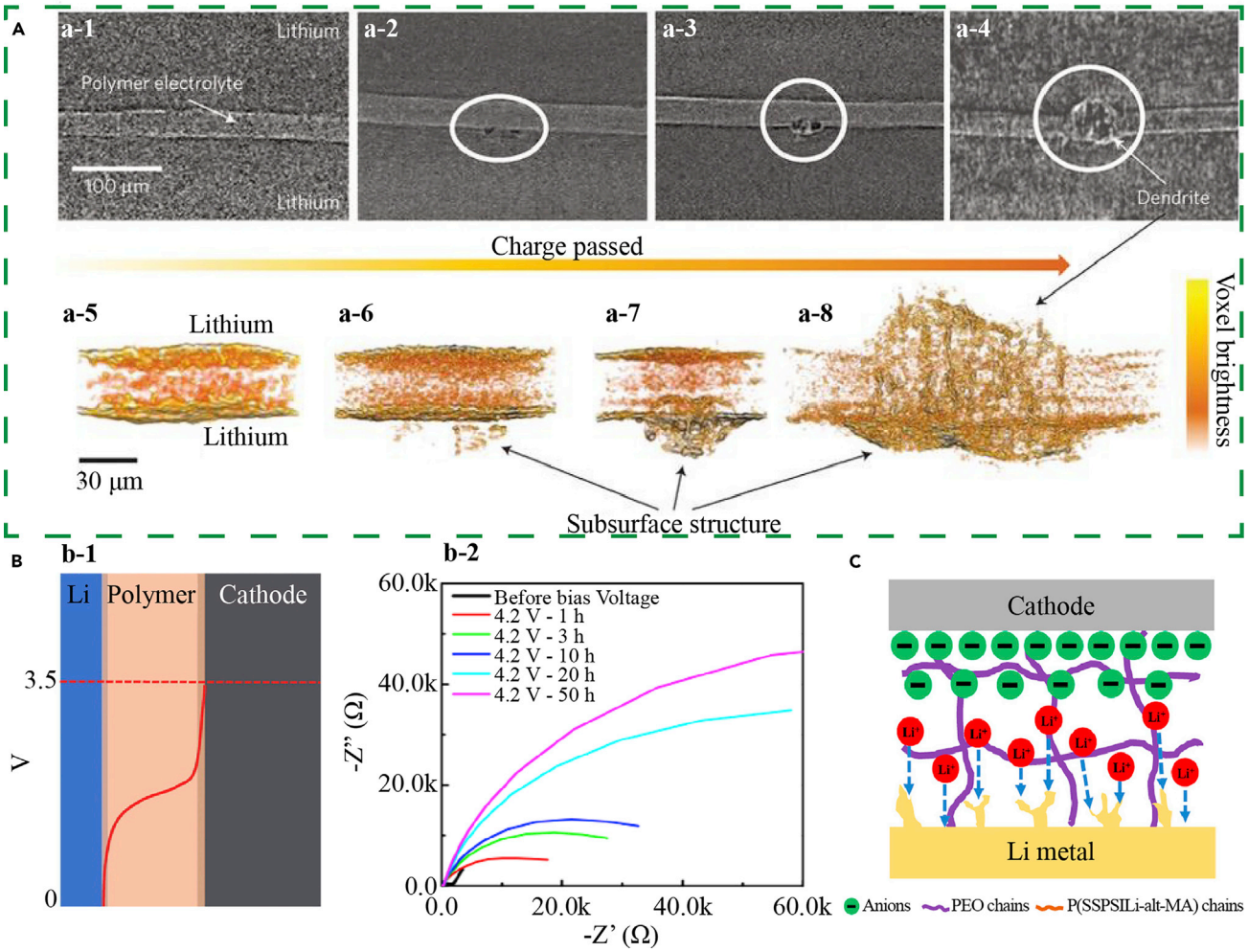

Figure 3. Dendrite Growth Triggered by Subsurface Structure and Redistributed Charges at Li|SE Interface

(A) Evolution of dendrite growth. X-ray tomography slides showing the cross-sections of a symmetric cell at various points of cycling with amount of charge passed, C: 0 C cm^{-2} (a-1), 9 C cm^{-2} (a-2), 84 C cm^{-2} (a-3), and short cell: 296 C cm^{-2} (a-4). Magnified, 3D reconstructed volumes of cells corresponding to uncycled cell, C = 0 C cm^{-2} (a-5), early stage of cycling, C = 9 C cm^{-2} (a-6), intermediate stage of cycling, C = 84 C cm^{-2} (a-7), and shorted cell, C = 296 C cm^{-2}. Adapted with permission from Harry et al.[26] Copyright 2013, Springer Nature.

(B) Redistributed charge induced dendrite growth. (b-1) Illustration of the electric potential profiles across the individual polymer electrolyte. (b-2) The impedance change of Li|polymer/Fe cell when applying a continuous bias voltage of 4.2 V on PEO. Adapted with permission from Zhou et al.[27] Copyright 2016, American Chemical Society.

(C) Schematics showing the charge distribution and dendrite issue in double-ion polymer electrolyte. Adapted with permission from Cao et al.[28] Copyright 2019, Elsevier Inc.

successfully minimized this concentration gradient using single-ion SPE (Figure 3C).[28] In normal dual-ion SPE, anions move freely and gather at the cathode side to form electric fields, which accelerates dendrite growth. In contrast, if the anions' mobility is limited (i.e., only Li^+ ion transfer), the electric field caused by the charge redistribution can be eliminated. As a result, dendrite growth caused by space charge can be successfully minimized.

Inorganic Solid Ceramic or Glass Electrolyte

Discontinuous Interface Contact Induced Dendrite Growth

Inorganic solid ceramic or glass electrolytes are rigid and have a high Li ion transfer number close to 1, which could effectively suppress dendrite growth. Nevertheless,

the continuous physical contact between Li and SCE is challenging, which could thus greatly affect Li deposition and dissolution behavior. This section therefore focuses on the effects of physical properties, such as physical contact, wetting property, porosity, and surface defects on dendrite growth.

The insufficient contact and voids at the interface caused by poor wetting between Li metal and SCE were regarded as the origin of huge interface resistance. As illustrated in Figure 4A, the physical contact between SCE and Li was more like a point-to-point case.[35] The inhomogeneous contact led to interface resistance and irregular Li ion flux distribution, which greatly decreased the CCD of SCE. Furthermore, the voids and holes at the interface allow for Li ion dendrite growth. Tsai et al. introduced a thin layer of Au buffer on the surface of polished SCE to improve the poor contact between the SCE and Li. As a result, the interface resistance was dramatically reduced and a cell free of short circuits was achieved.[35] On the other hand, the poor wetting property with Li, namely lithiumphobicity, was another significant contributor to insufficient contact (Figure 4B). Recently, Wu et al. have proved that the intrinsic lithiumphilicity characteristic of LLZO was reversed by Li_2CO_3 at the surface.[36] Based on their first-principle calculations, the intrinsic lithiumphilicity of LLZO was confirmed to have a contact angle between Li and Li_2CO_3-free garnets of less than 90°. However, in humid air, Li_2CO_3 was easily formed on the Gallium (Ga)-doped LLZO surface that had a contact angle as large as 127°. This negative effect was successfully eliminated by the removal of Li_2CO_3, which led to intimate contact between Li and SE.

In inorganic SCE, the porosity had a significant effect on the morphology, ionic conductivity, and mechanical strength. When the dendrite was formed at the Li|SCE interface, the pore character could greatly affect the propagation behavior of the Li dendrite inside SCE. Shen et al. investigated the relationship between the pores and the CCD with synchrotron X-ray tomography and proposed a microstructure-driven failure mechanism (Figure 4C).[37] As the sintering temperature increased from 1,050°C to 1,150°C, the porosity of the SCE decreased markedly while the underlying connectivity of the pore region increased. After the cells shorted and the CCD was achieved, the pores broadened because of the deposition of Li, based on the increased X-ray transparent volume. As a result, the connected pores accelerated dendrite growth in SCE and decreased the CCD.

The defects at the surface of SCE as another cause of dendrite growth were inevitable during the preparation process. Compared with the porous polycrystalline SCE, single-crystal SCE was believed to suppress dendrite growth.[39] However, in work by Chiang's group, despite the surface being polished to 4-nm root-mean-square roughness, a crack caused by Li propagation at a defect site of single-crystal SE was observed.[38] The Li deposition on the single-crystal SE was monitored with optical microscopy. As the deposition processed, a crack (white silhouette) appeared and gradually grew into the field of view, suggesting that a crack-tip stress propagated the crack during Li plating (Figure 4D). Based on a simplified geometry of Li filament within an SCE, an analytical model was developed to predict the maximum stress at the filament tip. The maximum stress was thermodynamically determined by the overpotential. An electro-chemo-mechanical model was then proposed to explain the dendrite growth in defects, whereby the minimum Li plating overpotential, defect size, and maximum stresses were considered. As a result, above the CCD the Li plating overpotentials and mechanical stresses reached values sufficiently large to extend surface defects. Their analysis suggested that the Li

Please cite this article in press as: Cao et al., Lithium Dendrite in All-Solid-State Batteries: Growth Mechanisms, Suppression Strategies, and Characterizations, Matter (2020), https://doi.org/10.1016/j.matt.2020.03.015

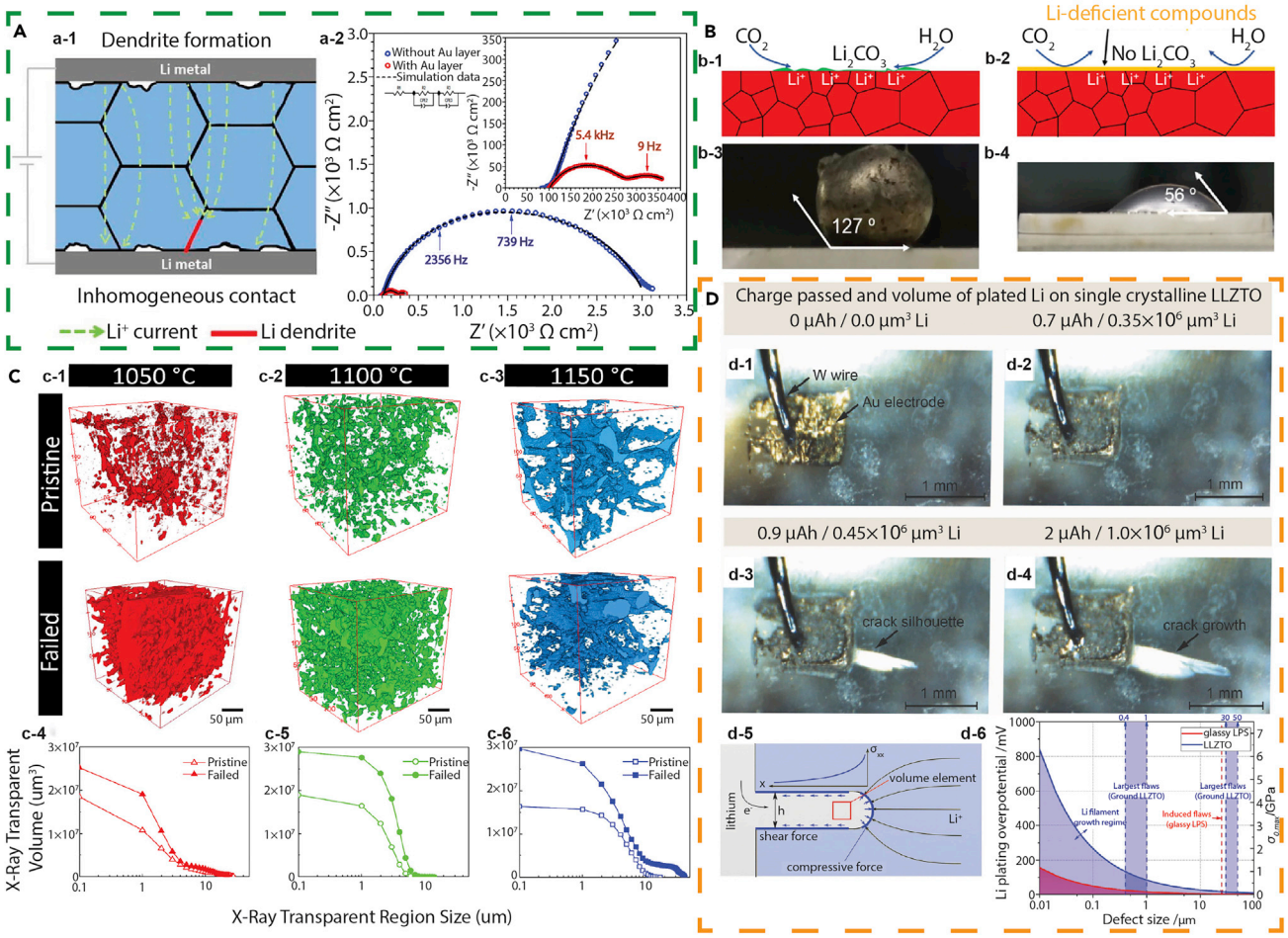

Figure 4. Dendrite Growth in Inorganic Solid Ceramic Electrolyte Triggered by Physical Properties

(A) Inhomogeneous contact. (a-1) Schematic illustrating dendrite formation due to the concentrated Li ion current caused by poor contact. (a-2) Impedance spectra for symmetric cell with and without Au buffer layer. Adapted with permission from Tsai et al.[35] Copyright 2016, American Chemical Society.

(B) Wetting property. Schematic showing the formation of Li_2CO_3 at the surface of SCE in humid air (b-1) and Li_2CO_3-free interface due to the protection of Li-deficient compound (b-2). Wetting of molten Li on SCE surface with (b-3) and without (b-4) lithiumphobic Li_2CO_3. Adapted with permission from Shi and Wu et al.[36] Copyright 2019, American Chemical Society.

(C) Pore property. Morphological changes in LLZO before and after the cell failed, investigated by X-ray tomographic reconstructions of void phase in the interior of SEs sintered at 1,050°C (c-1), 1,100°C (c-2), and 1,150°C (c-3). Changes in pore size distribution of SEs before and after the cell failed at 1,050°C (c-4), 1,100°C (c-5), and 1,150°C (c-6). Adapted with permission from Shen et al.[37] Copyright 2018, American Chemical Society.

(D) Defects. (d-1 to d-4) Optical microscopy images of single-crystal LLZTO with sputtered gold electrode during galvanostatic deposition of Li metal beneath the gold electrode at 5 mA cm^{-2} current density. Reproduced with permission. (d-5) Simplified schematic of a Li filament in solid electrolyte matrix. (d-6) Inverse square root dependence of Li plating overpotential and crack-extension stress on defect size. Adapted with permission from Porz et al.[38] Copyright 2017, Wiley-VCH Verlag GmbH & Co. KGaA, Weinheim.

plating stresses could propagate Li metal filaments via Griffith-like crack extension through brittle solid electrolytes.

Grain Boundary-Induced Li Dendrite Penetration

For most ceramic SEs, polycrystalline are more common and far more practical than single crystal. The grain boundaries that exist in polycrystalline SCEs have been reported to strongly affect the Li ion conductivity.[40] The boundaries were reported to play an important role in the Li deposition and propagation in polycrystalline SCEs.[41] Cheng et al. have directly observed that Li metal propagated through the web

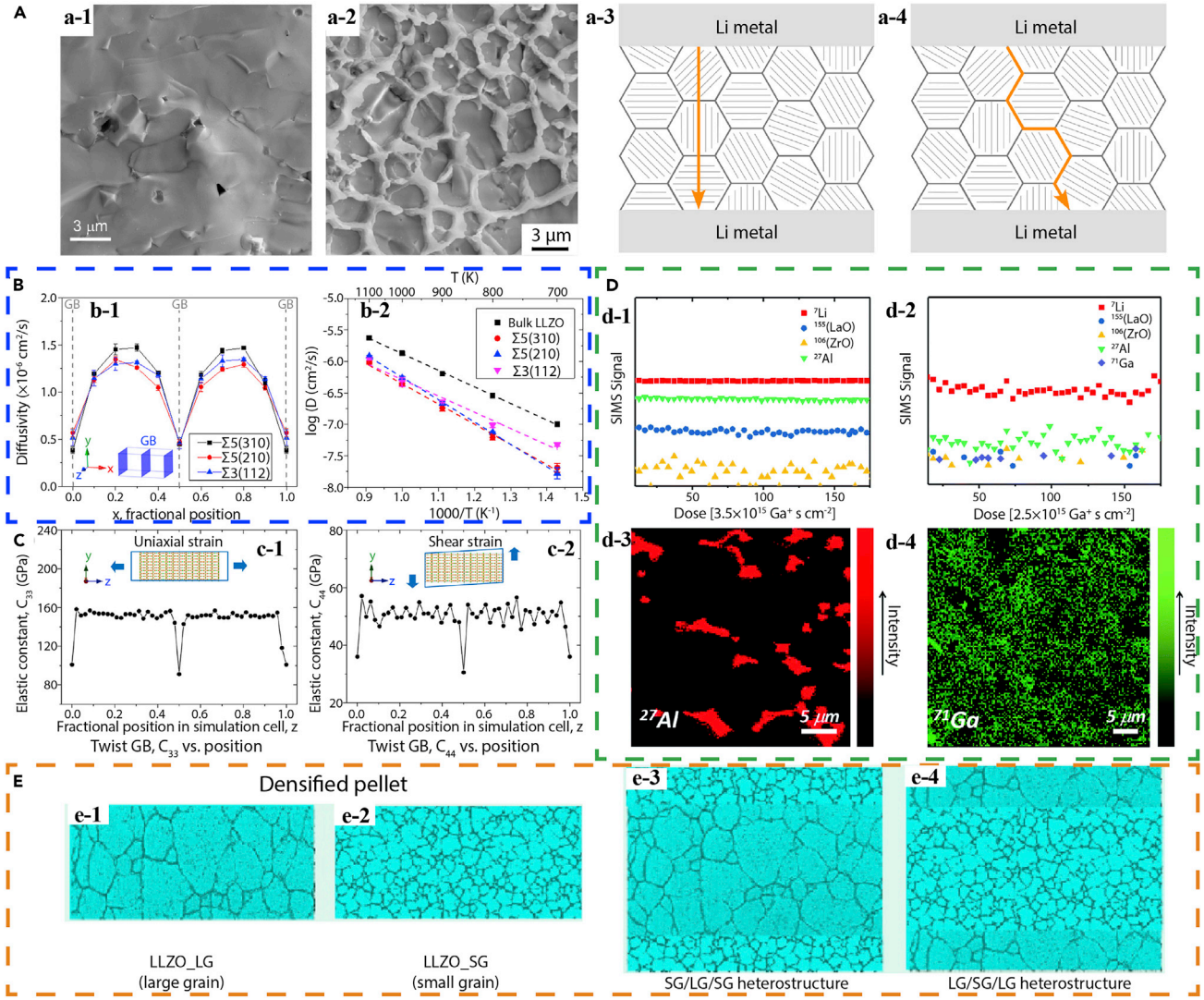

Figure 5. Grain Boundary Related Dendrite Growth

(A) Dendrite propagation through the grain boundary (GB). (a-1) SEM image of a fractured surface of uncycled $Li_{6.25}Al_{0.25}La_3Zr_2O_{12}$. (a-2) SEM image of the web structure in cycled $Li_{6.25}Al_{0.25}La_3Zr_2O_{12}$. Transgranular (a-3) and intergranular (a-4) type plating of Li metal through polycrystalline $Li_{6.25}Al_{0.25}La_3Zr_2O_{12}$. Adapted with permission from Cheng et al.[42] Copyright 2017, Elsevier Inc.

(B) Higher resistance at GB. (b-1) Calculated Li-ion diffusivity in Σ3(112), Σ5(210), and Σ5(310) type GB cells. (b-2) Arrhenius plots for Li-ion diffusivity in the GB regions compared with that in bulk $Li_{6.25}Al_{0.25}La_3Zr_2O_{12}$. Adapted with permission from Yu and Siegel.[43] Copyright 2017, American Chemical Society.

(C) Low elastic modulus. Calculated elastic constants C_{33} (c-1) and C_{44} (c-2) at 300 K as a function of position normal to the GB planes for the Σ5 twist GB cell. Adapted with permission from Yu and Siegel.[44] Copyright 2018, American Chemical Society.

(D) Different compositions in GB regions. Positive secondary ion depth profiles for Al-doped (d-1 and d-3) and Ga-doped (d-2 and d-4) $Li_7La_3Zr_2O_{12}$. Adapted with permission from Pesci et al.[45] Copyright 2013, The Royal Society of Chemistry.

(E) Grain size and grain distribution. Schematic of $Li_7La_3Zr_2O_{12}$ pellets with large grain (e-1), small grain (e-2), small||large|small grain (e-3), and large|small||large grain (e-4) heterostructures. Adapted with permission from Cheng et al.[46] Copyright 2015, American Chemical Society.

structure distributed grain boundaries in polycrystalline $Li_{6.25}Al_{0.25}La_3Zr_2O_{12}$ ceramic electrolyte (Figure 5A).[42] This evidence rendered a new intergranular type of Li propagation mechanism through polycrystalline SCEs, which was different from the common transgranular type. Driven by the electric field, Li could propagate through the grain boundary from one electrode to the other side. Significant experimental and theoretical efforts have been made to explain intergranular-type

propagation. Here we discuss possible reasons for the Li propagation through the grain boundaries, such as the grain boundary's higher resistance, lower shear modulus, and different composition compared with the bulk grain. Moreover, the amount of grain boundaries at the interface that can be adjusted by controlling the grain size also significantly affects the interface resistance.

The high local ionic resistivity of the grain boundary, relative to the bulk grain, was regarded as the main reason for dendrite growth.[40,43,47,48] Yu and Siegel theoretically investigated the energetics, composition, and transport properties of three low-energy (Σ3 and Σ5) symmetric tilt grain boundaries in $Li_7La_3Zr_2O_{12}$, where Σn (n = 3, 5) means one in n Zr sites overlap in coincident site lattice formed by the overlapping of two rotated grains.[43] They found that Li transport in the grain boundary was more difficult than the bulk grain and was sensitive to the temperature and grain boundary structure; in particular, the predicted activation energy for diffusion is 35% greater than in the bulk in Σ5-type geometry (Figure 5B). Meanwhile, Raj and Wolfenstine theoretically investigated the effect of grain boundary resistance on dendrite nucleation at Li and SCE interfaces.[47] They proposed that the local electro-chemo-mechanical potential of Li instigated the Li dendrite formation. Specifically, both the high local ionic resistivity of the grain boundaries and the physical irregularities in the shape of Li interface contributed to the dendrite growth.

The elasticity model proposed by Monroe and Newman failed to explain the dendrite growth in some SCEs. Inspired by this, Yu and Siegel performed molecular dynamics simulations to explore the shear modulus in the nanoscale regions near the grain boundary in LLZO.[44] They found that the shear modulus of the grain boundary was at most almost 50% smaller than in bulk grain (Figure 5C). In a plating process, Li preferred to accumulate in the softer regions near grain boundaries and stayed away from the stiffer bulk grain. This may explain the propagation of Li through the grain boundary network. They also noted that the shear modulus did not meet the criterion proposed in Monroe and Newman's model, although the grain boundary was significantly softer than the bulk.

Donor doping was often utilized to stabilize SCE to achieve better performance, but it has been reported that the distribution of dopant could affect the dendrite growth.[45] Pesci et al. investigated dendrite formation in Al- and Ga-doped LLZO, where the Ga-doped SCE displayed a 60% higher CCD than the Al-doped one.[45] Through a combination of techniques including secondary electron microscopy and secondary-ion mass spectrometry, they found that the dendritic features in Al-doped SCE were composed of Al and Li mixture, whereas those in Ga-doped SCE were exclusively composed of Li (Figures 5Dd-1 and 5Dd-2). The dendrites in both SCEs were detected as web-like structures spreading through the pellet. Figures 5Dd-3 and 5Dd-4 compare the distribution of doping elements. The Al element segregated at the grain boundaries in Al-doped SCE, whereas the Ga element was homogeneously distributed across grains and grain boundaries. These results demonstrated that Al segregation in the grain boundaries may facilitate the propagation of Li through the grain boundaries accompanied by a decreased CCD.

As the grain sizes in SCE range from a few to hundreds of micrometers, the grain orientations and grain boundary distribution may also affect the Li distribution. Cheng et al. investigated this issue in Al-substituted LLZO by designing pellets with different grain sizes and heterostructures.[46] Figure 5E displays four kinds of designed pellets, namely LLZO with large grain (LG), small grain (SG), SG|LG|SG heterostructure, and LG|SG|LG heterostructure. As depicted, the small grain had a

relatively large number of grain boundaries at the interface between Li and SCE, which was verified by the smaller interface resistance. The potential effects of individual grain orientation as well as the misorientations of neighboring grains were eliminated. These studies confirmed that the microstructure at the surface of SCE strongly influenced the interface resistance. The surface layer was suggested to own small grains and multiple grain boundaries due to the enhanced ionic transport.

Li Plating inside the Solid Ceramic or Glass Electrolyte

Ideal SEs have high ionic conductivity and extremely low electronic conductivity. Driven by the electric potential, the reduction of Li ions to Li metal only happened at the Li|SE interface. However, for some SCEs the electronic conductivity was too high that the reduction of Li ions could happen directly inside the SCE. Moreover, some excess electrons and negative charges might be trapped inside the SCE by the pores, which would directly reduce the Li ions. These findings revealed the primary reason for dendrite formation inside SEs.

Recently, Han et al. proposed that the relatively high electronic conductivities of LLZO and Li_3PS_4 were the origin of dendrite formation.[49] As shown in Figures 6Aa-1 and 6Aa-2, both LLZO and Li_3PS_4 exhibited temperature-dependent electronic conductivities in the range 10^{-9}–10^{-7} S cm^{-1}, which was much higher than that of lithium phosphorus oxynitride (LiPON) (10^{-15}–10^{-12} S cm^{-1}), a well-known dendrite-free SCE. The study showed that the electronic conductivity of LLZO reached 10^{-6} S cm^{-1} during Li plating.[50] The high electric conductivity rendered the possibility of Li ions to combine with electrons to form dendrites inside the SCE. Using neutron depth profiling (NDP), the nucleation and growth of Li dendrites inside the SCE were visualized in real time. As depicted in Figures 6Aa-3 and Aa-4, the amount of Li in Li|LLZO|Cu and Li|Li_3PS_4|Pt cells transported from the counter electrodes (Li) deviated from the cumulative charge after a period of plating. Compared with the cumulative charges, the relatively low amount of Li indicated dendrite formation in the deep and undetectable region inside the SCE. The changes of Li concentrations in SCE during plating are compared in Figures 6Aa-5 and 6Aa-6, where the Li content continuously increased during plating. The accumulated Li was independent of depth, suggesting no Li concentration gradient. The research thus highlighted that Li directly nucleated inside the SCE, which was inconsistent with the conventional understanding that dendrites grow directionally from one electrode to the other. Their findings explained the rapid short circuit in SCE.

Despite the intrinsic electronic conductivity of SCEs, the electrons from negative charges such as O^{2-} and the excess electrons trapped by the pore and crack surface also accelerated the direct reduction of Li ions inside the SCEs.[51,52] Aguesse et al. found the existence of island-like black spots inside the SCE after cycling, which was further proved to be a Li cluster (Figures 6Bb-1 and 6Bb-2).[51] It was explained that Li ions gain electrons from the oxygen backbone of the ceramic in a slow degradation process. As a result, four scenarios for metallic Li formation were proposed (Figure 6Bb-3): (1) Li metal plated on electrode; (2) Li metal deposited on dendrite; (3) Li metal formation (electron transfer from oxygen framework); and (4) Li metal formation (electron transfer from residual conductivity). Tian et al. computationally investigated the Li nucleation tendency in LLZO, where the trapped excess electrons induced Li deposition on the pore surface.[52] In their work, there were excess electrons trapped around the La atoms on the surface of cubic LLZO and dispersed on the surface of tetragonal LLZO. These excess electrons were thermodynamically favorable for reducing Li ions to Li metal (Figure 6C).

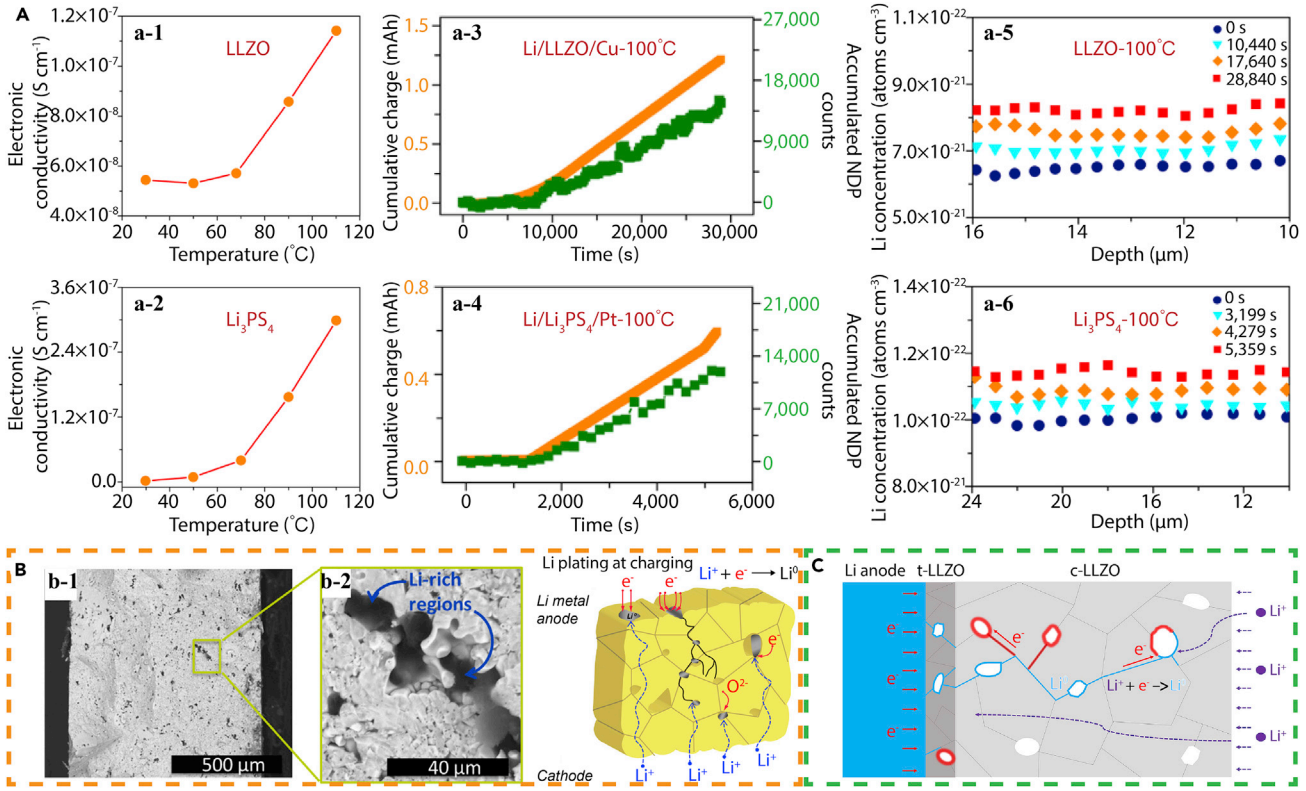

Figure 6. Direct Reduction of Li Ion Inside the SEs by the Electrons

(A) Intrinsic electric conductivity. Temperature-dependent electronic conductivity of LLZO (a-1) and Li_3PS_4 (a-2). Correlation between cumulative charges (origin line) and the accumulated NDP counts (green dots) in the total region of the Li|LLZO|Cu cell (a-3) and the Li|Li_3PS_4|Pt cell (a-4) at 100°C. At 100°C, Li concentration profiles in LLZO (a-5) and Li_3PS_4 (a-6) at different times during plating process to obtain visualization of the depth distribution of dendrites in SEs. Adapted with permission from Han et al.[49] Copyright 2019, Springer Nature.

(B) Li cluster formation due to reduction by electrons from oxygen network and residual electronic conductivity. (b-1) Cross-section SEM image of a cycled pellet obtained by BSED to show the black points inside the SE. (b-2) SEM image with higher magnification to show the Li-rich region in the pores. Schematic on the right shows a cross-section in SCE where the potential Li ion reduction mechanisms are proposed. Adapted with permission from Aguesse et al.[51] Copyright 2017, American Chemical Society.

(C) Schematic of metallic Li formation on the pore surfaces inside of c-LLZO due to the electron pathway provided by the pore surfaces and possible grain boundaries. Adapted with permission from Tian et al.[52] Copyright 2018, Elsevier Inc.

Interphase Effect on Dendrite Growth

Most SCEs are intrinsically thermodynamically unstable against Li metal, which has been demonstrated both computationally and experimentally. The reaction between the SCEs and Li leads to the formation of interphase layers with different properties, which play a significant role in the behavior of the cell. In this section, we focus on the interphase effect on dendrite growth.

Recently, Wang et al. proposed that highly stable SCE against metal anodes accelerated fast dendrite formation, while the interphase layer with high ionic conductivity and low electronic conductivity effectively suppressed dendrite formation.[53] As depicted in Figure 7A, electrochemical impedance spectra (EIS) was utilized to verify the chemical instability between the SCE and metal anode before cycling. The impedance gradually increased with aging, suggesting the formation of an interphase layer. During cycling, the Li-SCE-Li cell exhibited significantly enhanced polarization, but no short circuit occurred. However, the Na-SCE-Na cell shorted after only eight cycles. Employing time-of-flight secondary-ion mass spectrometry (TOF-SIMS), a thick interphase layer (red region) in the Li-SCE interface was confirmed,

Please cite this article in press as: Cao et al., Lithium Dendrite in All-Solid-State Batteries: Growth Mechanisms, Suppression Strategies, and Characterizations, Matter (2020), https://doi.org/10.1016/j.matt.2020.03.015

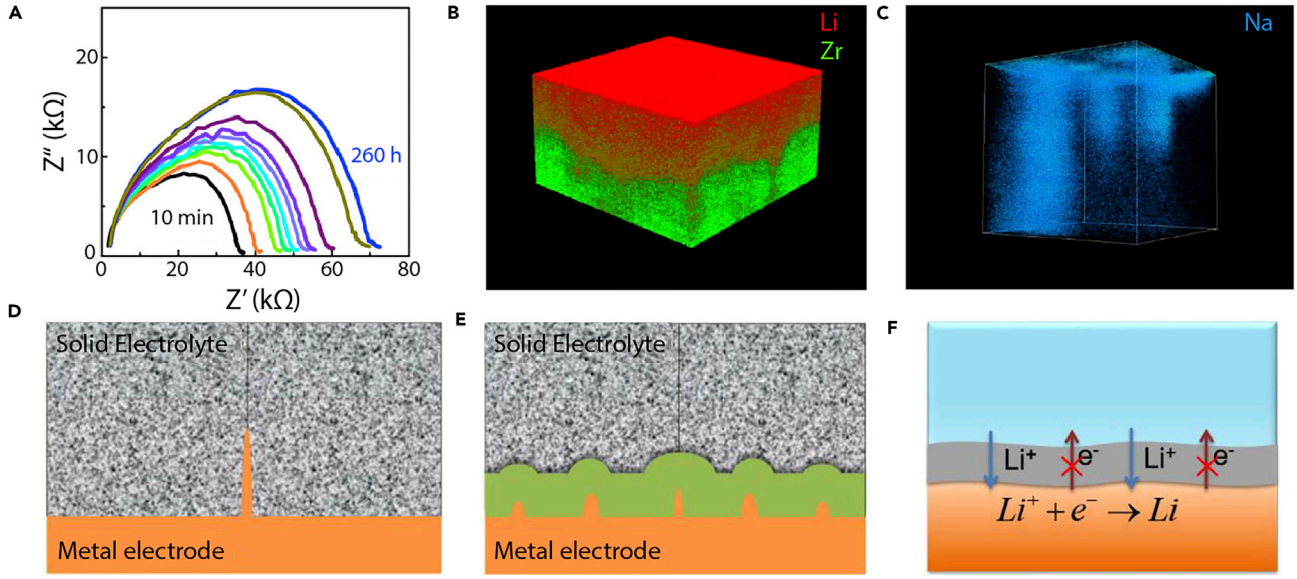

Figure 7. Dendrite Growth at the Interface with No Artificial SEI

(A) Impedance spectra of Li-$Li_{1.15}Y_{0.15}Zr_{1.85}(PO_4)_3$-Li cell at different aging times: 10 min, 30 min, and 1, 2, 5, 18, 23, 46, 68, and 260 h.

(B and C) 3D view of Li (Li^+), Zr (Zr^+) (B), and Na (Na^+) (C) distribution in the TOF-SIMS sputtered volumes of $Li_{1.15}Y_{0.15}Zr_{1.85}(PO_4)_3$ (B) and $Na_3Zr_2(SiO_4)_2PO_4$ (C) after cycling.

(D and E) Schematics showing dendrite growth in SE with high chemical stability against Li (D) and SE with interphase (E).

(F) Schematic of the ideal interphase layer with high ionic conductivity and low electric conductivity.

Adapted with permission from Wang et al.[53] Copyright 2018, American Chemical Society.

whereas in the Na-SCE-Na cell, the dendrite penetrated the SCE and only a thin layer formed between Na and SCE layers (Figures 7B and 7C). Thermodynamic analysis was conducted to explain the interphase effect on dendrite growth. Due to the unity ionic transference number, the relatively higher chemical stability of SCE with Li rendered a notably lower consumption of Li during cell operation. Meanwhile, a much larger curvature at expanded dendrite tips in confined spaces in SCE caused an enhanced electric driving force. Both aforementioned changes aggravated the growth of the dendrite (Figure 7D). With the help of an interphase layer, the Gibbs free energies for electrochemical reduction of SCE and Li plating can reach an equilibrium, which consequently prevented the fast dendrite growth (Figure 7E). The authors proposed that an ideal interphase layer should have low electronic conductivity and high ionic conductivity to enable the uniform Li plating and stripping, as illustrated in Figure 7F.

STRATEGIES OF LI DENDRITE SUPPRESSION

Based on the Li dendrite growth mechanisms, various solutions have been proposed to alleviate dendrite growth. For example, to suppress dendrite growth in OLEs, investigators have attempted to stabilize the SEI layer by various methods such as introducing various hosts, adding additives, increasing the concentration of the electrolyte salt, designing artificial SEI at the electrode|electrolyte interface. However, due to inherent differences, the strategies of Li metal stabilization in OLEs cannot be directly applied to SEs. For SPEs, because of their soft nature, the interface contact was much more uniform than SCEs. Therefore, for SPEs, reinforcing the mechanical strength was more urgent than improving the interface contact to suppress the dendrite. Conversely, the rigid SCEs have sufficient mechanical strength but poor interface contact. Therefore, the interface between the SCE

and Li was more critical in the fabrication of dendrite-free and high-performance ASLBs. Feasible strategies, such as the optimization of SCEs, modification of Li metal, and indirectly or directly introducing a buffer layer at the interface have been applied to enable a dendrite-free cell. In the following subsections, we discuss the most common strategies that have been employed in ASLBs for dendrite suppression.

Polymer-Based Composite Solid-State Electrolyte to Suppress Li Dendrite

Compositing SPE with various additives is a common strategy to enhance its mechanical strength and ionic conductivity.[32] The additives, as known as fillers, were not only restricted to ionic conductive materials, but the non-ion-conductive ceramic and additional polymer were also used. The size ranged from nano- to micrometer and the morphology from zero-dimensional (0D)[54,55] to one-dimensional (1D),[56,57] two-dimensional (2D),[58] and three-dimensional (3D).[59] Some properties of the fillers, such as electron insulation and chemical and thermal stability, are highly desired.

Hybrid Electrolyte Compositing with Non-ion-conductive Ceramic Filler

Non-ion-conductive ceramic fillers were widely applied in polymer electrolyte to reinforce the mechanical strength and ionic conductivity of the SPE. Recently, Tang et al. introduced 2D vermiculite clay sheets into the PEO-based SPE to prompt the mechanical strength and ionic conductivity (Figure 8A).[58] Compared with 0D and 1D fillers, 2D geometry had higher surface area and could anti-deform. Freestanding PEO-based SPE film was prepared by adding exfoliated 2D vermiculite clay nanosheets. After adding fillers, the tensile modulus of the SPE doubled from 6.8 MPa to 13.1 MPa along with much higher tensile strain before fracture. Compared with the morphologies of Li electrodes after cycling measurement, the SPE with 2D fillers had a dendrite-free surface. A similar strategy for enhancing the SPE by introducing stiff fillers was also reported by Lin et al.[59] As illustrated in Figure 8B, a stiff mesoporous SiO_2 aerogel was introduced into the SPE, which not only reinforced the mechanical strength but also offered sufficient surface for strong anion adsorption. As a result, there was around a 10-fold increase in modulus for the silica aerogel-reinforced SPE. Interestingly, the modulus increased slightly with the increase in temperature, which was superior over traditional SPE whose mechanical strength degraded at higher temperatures. Other representative works reported SPE reinforcements such as SiO_2 nanospheres,[60,61] vertically aligned anodized Al_2O_3 scaffold,[62] and 2D boron nitride nanosheets,[63] which further confirmed that the addition of non-ion-conductive fillers helped the SPE with dendrite suppression.

Introducing additional polymer into the original SPE was also an effective way to suppress dendrite growth. Zeng et al. designed a novel SPE with an interpenetrating network of poly(ether-acrylate) (ipn-PEA) via photopolymerization of ion-conductive PEO and branched acrylate (Figure 8C).[16] Along with its plasticity and rigidity, this SPE exhibited high ionic conductivity (0.22 mS cm^{-1} at room temperature) and high mechanical strength (12 GPa). When the ipn-PEA was matched with Li metal, the rigid network supported high pressure to reshape the Li plating and stripping behavior. In the meantime, the ductile PEO avoided the tradeoff in ionic conductivity. Khurana et al. reported a crosslinked polyethylene-poly(ethylene oxide) SPE with excellent resistance to dendrite growth.[18] Interestingly, the modulus of their SPE was about 1.0×10^5 Pa at 90°C, which was lower than the required value from theoretical predictions. Yang et al. proposed that the structure of the polymer additives also affected the contact issue between the SPE and Li.[64] As illustrated in Figure 8D,

Please cite this article in press as: Cao et al., Lithium Dendrite in All-Solid-State Batteries: Growth Mechanisms, Suppression Strategies, and Characterizations, Matter (2020), https://doi.org/10.1016/j.matt.2020.03.015

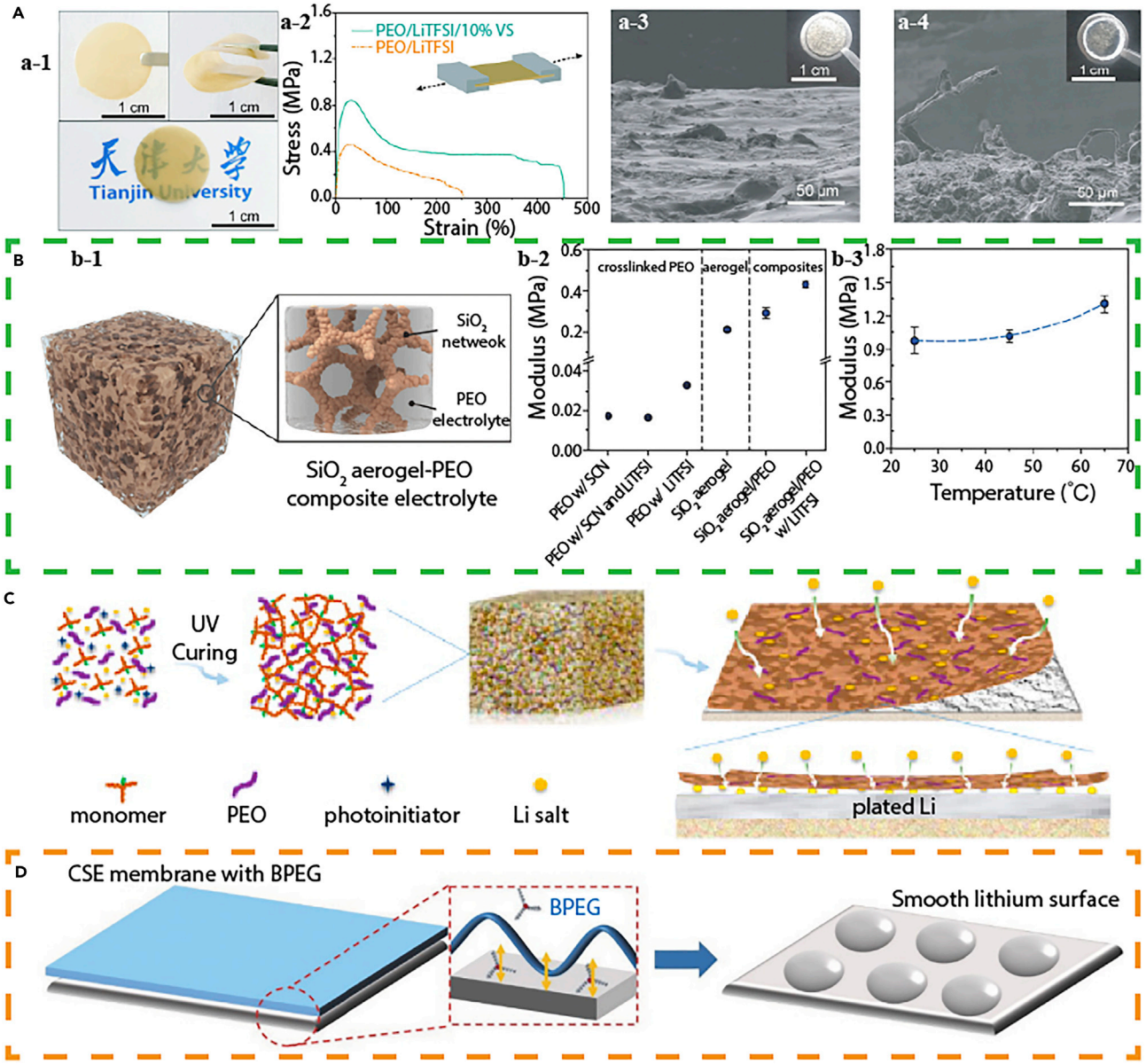

Figure 8. Polymer Electrolyte with Non-Ion-Conductive Ceramic Fillers

(A) 2D fillers. (a-1) Photographs of the composite SPE film. (a-2) Stress-strain curves of the SPE with and without fillers under tensile test to show the enhanced mechanical stability. The cross-section SEM images of Li electrode in cells using SPE with fillers (a-3) and SPE after cycling (a-4) show dendrite suppression. Adapted with permission from Tang et al.[58] Copyright 2018, Wiley-VCH Verlag GmbH & Co. KGaA, Weinheim.

(B) 3D fillers. (b-1) Schematic showing the SiO_2-aerogel-reinforced SPE. The magnified drawing shows the detailed microstructure of the composite electrolyte. (b-2) Elastic modulus of the crosslinked PEO with SCN, crosslinked PEO with both SCN and LiTFSI, crosslinked PEO with LiTFSI, SiO_2 aerogel, SiO_2-aerogel-PEO composite, and SiO_2-aerogel-PEO composite with LiTFSI. (b-3) Modulus of the SiO_2-aerogel-PEO composite as a function of temperature. Adapted with permission from Lin et al.[59] Copyright 2018, Wiley-VCH Verlag GmbH & Co. KGaA, Weinheim.

(C) Additional polymer. Schematic showing the preparation process of the ipn-PEA electrolyte and the proposed Li deposition behavior. Adapted with permission from Zeng et al.[16] Copyright 2016, American Chemical Society.

(D) Effect of polymer additive with planar structure. Proposed Li deposition behavior with the introduction of planar oligomer. Adapted with permission from Yang et al.[64] Copyright 2017, Wiley-VCH Verlag GmbH & Co. KGaA, Weinheim.

the PEO with high molecular weights typically featured curvy chains with large curvature radii and tended to tangle up with other chains. Thus, voids existed between the PEO chains and the Li anode accelerated the growth of dendrite. The addition of

oligomers filled into those voids led to better contact. Compared with the 1D linear oligomers, planar oligomers with 2D structure avoided entanglement with the linear chains, which created a large area of "softer contact" with Li.

Hybrid Electrolyte Compositing of Ion-Conductive Filler

Compositing the ionic conductive ceramics into polymer electrolytes was a successful strategy to combine the merits of both SCE and SPE.[56,59,65–68] The rigid SCE reinforced the SPE to achieve a high mechanical strength and improved ionic conductivity, while SPE had a soft contact with Li to decrease the interface resistance. According to the content ratio of SCE to SPE, the composite SEs were classified into "ceramic-in-polymer" (CIP), "intermediate," and "polymer-in-ceramic" (PIC), whereby the ionic conductivity and mechanical strength were dependent on the makeup of the electrolyte.[69] It was vital to balance the ionic conductivity, interfacial contact, rigidity, and softness to achieve optimized performance for composite SE.

Recently, Huo et al. designed a composite SE with hierarchical CIP|PIC|CIP structure, which effectively suppressed dendrite formation.[55] They integrated $Li_{6.4}La_3Zr_{1.4}Ta_{0.6}O_{12}$ (LLZTO) in different sizes with polymer at different ratios to fabricate the CIP and PIC. As shown in Figure 9A, CIP electrolyte with 20 vol % 200-nm LLZO exhibits best flexibility, while PIC electrolyte with 80 vol % 5-μm LLZTO exhibits the highest tensile strength of 12.7 MPa. Appreciating the rigid property of LLZTO, PIC electrolyte was strong enough to suppress dendrite formation, but intimate interfacial contact was still lacking. On the contrary, CIP electrolyte had good interfacial contact but failed to suppress dendrite growth. As illustrated in Figure 9Aa-4, the sandwich-type electrolyte had the merits of both CIP and PIC and displayed the best performance.

Besides the reinforcement in mechanical strength, the composite SE exhibited a higher Li ion transference number as compared with SPE. It has been reported that SE with a high ion transference number can effectively prevent Li dendrite formation.[72,73] However, most of the SPE suffered from a low ion transference number (<0.5), which was attributed to the high movement of Li salt anions. Zhao et al. proposed an anion-immobilized composite SE whose Li ion transference number was as high as 0.58.[70] The polymer matrix and ceramic fillers tethered the anions and constricted anion movement, which rendered the uniform distribution of space charges and Li ions (Figure 9B). As a result, the electric field caused by the redistribution of space charge was relieved, which rendered a dendrite-free anode. Blocking the movement of anions from anode to cathode was another effective strategy to eliminate the negative effect of low ion transference number. Zhou et al. designed a composite solid electrolyte with a polymer|ceramic|polymer sandwich architecture, in which the anions were blocked by the ceramic interlayer (Figure 9C).[27] By using this composite solid electrolyte, the double-layer electric field at the Li|polymer interface was successfully reduced. The soft polymer enabled intimate contact with the Li, which led to a more homogeneous Li ion flux at the interface.

In addition to the aforementioned strategies, Whiteley et al. proposed an interesting self-optimizing mechanism for composite SE using amine-based polymer.[71] In their work, they termed the growth of Li along the particle boundaries of SCE "interparticle Li growth" (IPL). The IPL forced the SCE particles out into the widely existing void space and continued to grow until short circuit occurred (Figure 9D). In contrast, benefiting from the self-healing property, the SCE|polymer system was adaptive to

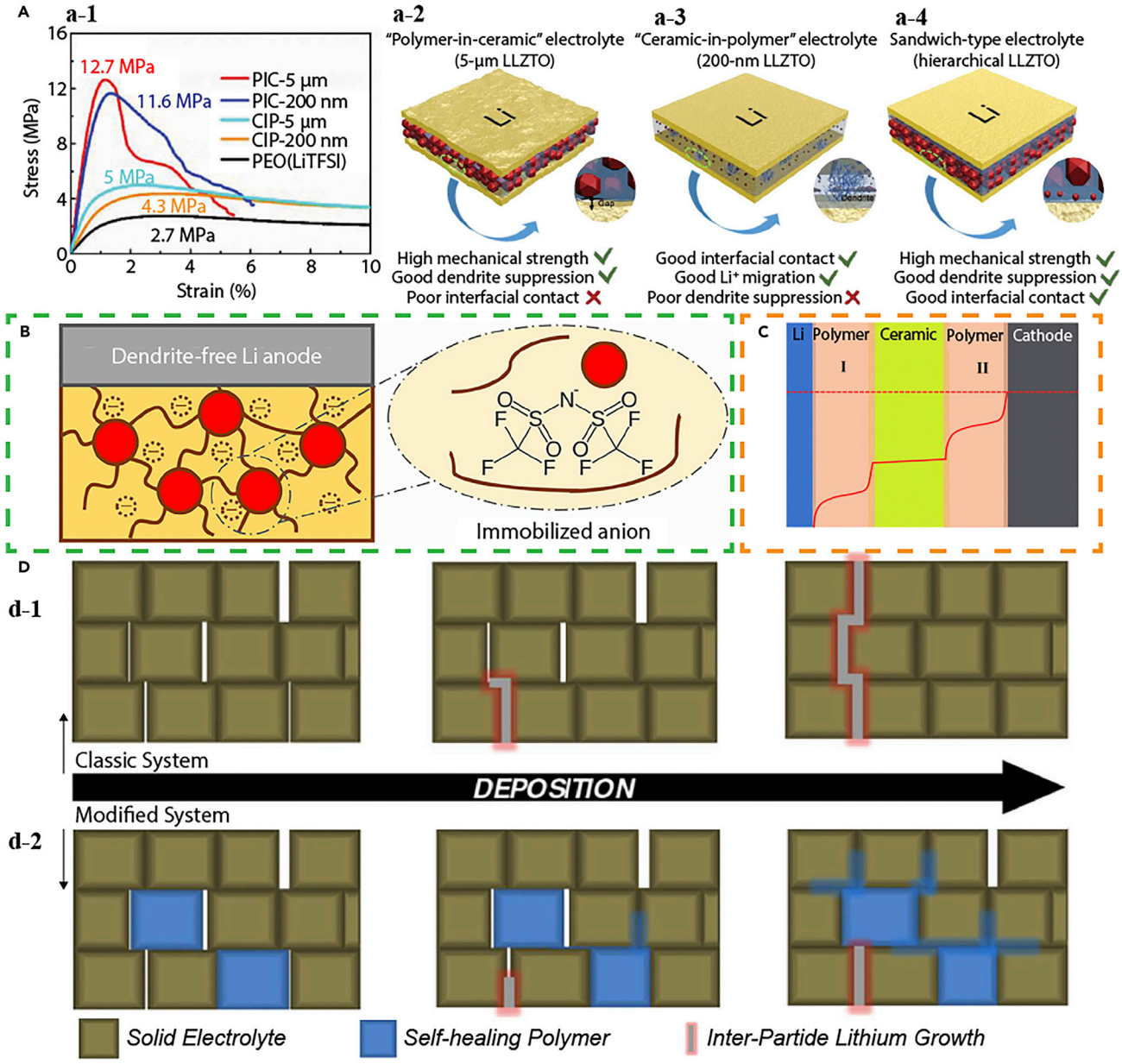

Figure 9. Polymer Electrolyte with Ion-Conductive Ceramic Filler

(A) Composite electrolyte with hierarchical "ceramic-in-polymer" and "polymer-in-ceramic" structures in dendrite suppression. (a-1) Stress-strain curves of different SPE. Schematic illustrations of PIC electrolyte with 5-μm LLZTO (a-2), CIP electrolyte with 200 nm LLZTO (a-3), and sandwich-type electrolyte and corresponding property (a-4). Adapted with permission from Huo et al.[55] Copyright 2019, Wiley-VCH Verlag GmbH & Co. KGaA, Weinheim.

(B) Polymer electrolyte with higher ion transference number to inhibit dendrite formation. Schematic illustrates the immobilization of anions tethered by polymer chains and $Li_{6.75}La_3Zr_{1.75}Ta_{0.25}O_{12}$ particles. Adapted with permission from Zhao et al.[70] Copyright 2017, National Academy of Sciences of the United States of America.

(C) Ceramic interlayer to block the movement of anions. Schematic illustrates the electric potential profile across the polymer-ceramic-polymer sandwich electrolyte. Adapted with permission from Zhou et al.[27] Copyright 2016, American Chemical Society.

(D) Self-healing composite electrolyte. Schematic of the proposed mechanisms to illustrate dendrite growth through the grain boundaries in classic system of SCE (d-1) and self-healing of polymer to suppress dendrite growth in modified system (d-2). Adapted with permission from Whiteley et al.[71] Copyright 2017, IOP Publishing Ltd.

slow growth or blocked the growth of IPL. The polymer was able to grow along the SCE boundaries and relieve the stresses generated in the system, which enabled a more stable interface. This proposed mechanism properly explained why the self-healing polymer worked better at higher temperature.

Optimization of Solid Electrolyte and Li Metal

Although compositing SPE and SCE addressed the dendrite problem, the ionic conductivity was sacrificed to some extent so that most composite SEs-based ASLBs needed external heating to achieve comparable performance with LIBs using OLEs. Moreover, the thermal stability window of the composite SEs was also narrow in comparison with pure SCE. It is important to optimize the SCE's physical and chemical properties to avoid dendrite formation. On the other hand, the modification of Li metal is another effective strategy to stabilize Li plating and stripping.

Optimization of Solid Ceramic and Glass Electrolyte

According to the scenarios proposed in Figure 1B, dendrites usually grew along with the defects, which were defined as any non-uniformity in SCE, including voids, cracks, grain boundaries, impurity precipitates, and local non-stoichiometry.[74] Most SCE experienced a tablet process to achieve a thin film from the SCE powder, which inevitably introduced defects. Decreasing the defect density of the polycrystalline SCE was vital to avoid dendrite formation.

Single-crystal SCE could fundamentally eliminate the effect of grain boundaries and voids. Kataoka et al. successfully fabricated centimeter-sized single crystals of garnet-type SCE using the floating zone method (Figure 10A).[39] The transparent pellet had a very smooth surface without grain boundaries and voids. As a result, this single-crystal SCE exhibited a high ion conductivity of 10^{-3} S cm^{-1} at room temperature and high CCD of 0.5 mA cm^{-2}. Unfortunately, the single-crystal SCE cannot sustain higher current density due to other factors such as poor contact with electrodes. However, reduction of grain boundaries and voids postponed dendrite growth and time to short circuit.

The relatively high cost and complex synthesis techniques further limited the application of single-crystal SCEs. Polycrystalline SCEs were easier and more cost-effective to fabricate. Therefore, researchers optimized the densification conditions to achieve denser polycrystalline SCEs. Several pressing strategies, such as uniaxial cold or hot pressing and isostatic pressing, have been applied, whereby the conditions notably affected the result.[80–82] It has been reported that higher hot-processing temperature has significantly increased the relative density of the garnet-type SCE pallets from 91.5% to 99.1%, which decreased the grain boundary resistance and enhanced ionic conductivity.[37,83] However, the increase in sintering temperature may generate by-products with low conductivity in Li_2S-P_2S_5 glassy electrolyte, which could decrease the CCD.[84] Yi et al. reported metallo-organic-derived flame-made nanoparticles to overcome the processing challenges in densification. The input energy for densification was highly reduced and the dwell time at sintering temperature was shortened 10- to 40-fold. The SCE with low defect density often had high translucency, induced by the decreased optical scattering from defects. The dense and fine-grained materials could provide the SCE film with flexibility and capability to avoid crack propagation (Figure 10B).[75]

In addition to the above strategies aiming to achieve dense SCE, porous structures have been reported to inhibit dendrite formation. Xu et al. designed a trilayer

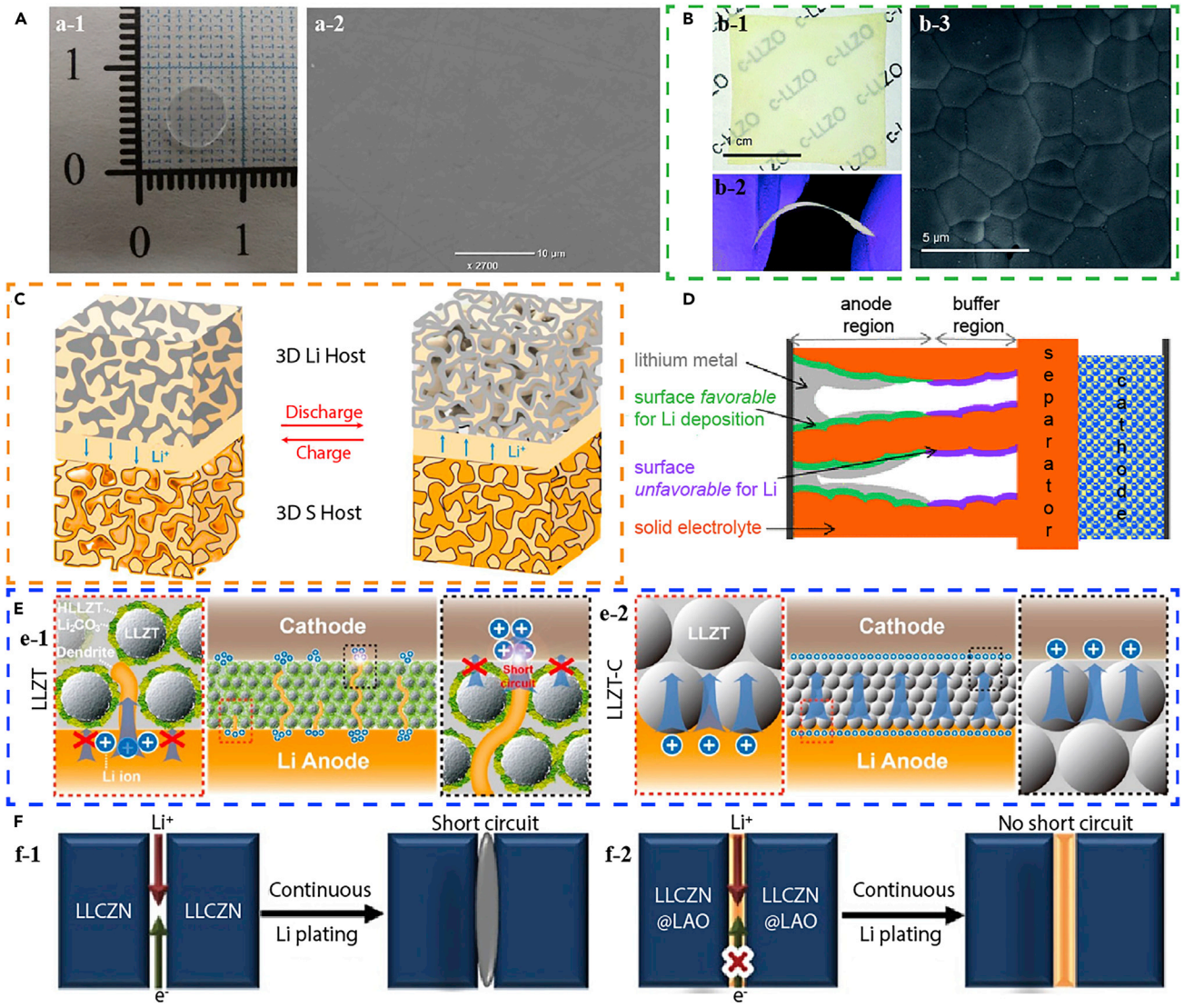

Figure 10. Dendrite Suppression through Optimizing the SCE

(A) Single-crystal SCE to eliminate the effect of grain boundaries and voids. Photograph (a-1) and surface SEM image (a-2) of the single-crystal $Li_{6.5}La_3Zr_{1.5}Nb_{0.5}O_{12}$. Adapted with permission from Kataoka et al.[39] Copyright 2018, Springer Nature.

(B) Densified SCE with low porosity. (b-1 and b-2) Photographs of the $Li_7La_3Zr_2O_{12}$ film show obvious translucency and decent flexibility. (b-3) Surface SEM of the $Li_7La_3Zr_2O_{12}$ film shows the compact contact of the grains. Adapted with permission from Yi et al.[75] Copyright 2016, The Royal Society of Chemistry.

(C) SCE with porous structure to inhibit dendrite growth during cycling. Adapted with permission from Xu et al.[76] Copyright 2018, Elsevier Inc.

(D) Model for ideal porous SCE. Cell schematic (not to scale) illustrating porous solid electrolyte designed with anode and buffer regions to regulate the deposition of Li metal. Adapted with permission from Thomas-Alyea.[77] Copyright 2018, IOP Publishing Ltd.

(E) Impurity removal to avoid dendrite propagation. Schematics show the impurity-caused dendrite growth in $Li_{6.25}La_3Zr_{1.5}Ta_{0.5}O_{12}$ (e-1) and dendrite-free in carbon-treated $Li_{6.25}La_3Zr_{1.5}Ta_{0.5}O_{12}$ (e-2). Adapted with permission from Li et al.[78] Copyright 2018, American Chemical Society.

(F) Additional phase to decrease the electric conductivity. (f-1) Schematic illustrating dendrite growth along the grain boundary of $Li_7La_{2.75}Ca_{0.25}Zr_{1.75}Nb_{0.25}O_{12}$ due to the enhanced electronic conductivity. (f-2) Schematic illustrates that dendrite suppression due to the introduction of insulating $LiAlO_2$ buffer layer at the grain boundary reduced the electron transfer. Adapted with permission from Song et al.[79] Copyright 2019, Wiley-VCH Verlag GmbH & Co. KGaA, Weinheim.

garnet-based ASLB with porous structures to stabilize Li (Figure 10C).[76] Li was infiltrated into the porous garnet framework and seamless contact was achieved by introducing ZnO at the solid electrolyte surface. In their design, the 3D porous structure enabled a high contact area, which decreased the local current density when an

areal current was applied. Meanwhile, the volume change of Li during plating and stripping can be locally confined by the garnet framework. As a result, dendrite-free ASLBs with high mass loading of Li were achieved. Based on the porous Li design, Thomas-Alyea presented an electrochemical model for the cell with porous solid anolyte (Figure 10D).[77] In the porous structure, there was space to accommodate Li volume expansion during plating, and the local surface overpotential was small. However, the low charge-transfer resistance of the porous electrode had a high reaction rate next to the separator, which imparted stress against the separator and eventually caused dendrite penetration. From these results, the author proposed the optimized porous SCE for Li deposition, whereby a buffer region was introduced between the porous part and separator. In this region, the porous SCE was coated with a layer of material with poor ionic conductivity and high surface energy, which avoided the fast Li deposition in the pores adjacent to the separator.

Removal of the impurity with poor ionic conductivity in SCE was another strategy to avoid dendrite growth. The widely studied garnet electrolytes were easily contaminated by moisture to form Li ion-insulating Li_2CO_3 surface layer, which could bring huge interface resistance and inhomogeneous Li deposition as aforementioned (Figure 10E).[78] The most frequently used strategy was high-temperature annealing in inert atmosphere, which triggered the decomposition of Li_2CO_3. Beyond this, Goodenough's group introduced an approach to remove the Li_2CO_3 with carbon as the reaction of $2Li_2CO_3 + C \rightarrow 4Li^+ + 3CO_2 + 4e^-$. As a result, the garnet without Li_2CO_3 exhibited enhanced wettability with Li metal and extended the electrochemical stability window. The interfacial resistance was also reduced to the levels of LIBs using liquid electrolyte.[78]

It is worth noting that not all the additional phases in SCE can decrease the performance. Introducing proper interphase material could also effectively avoid dendrite formation. Song et al. coated a thin layer of $LiAlO_2$ on the grain surface of garnet, which greatly improved the CCD (Figure 10F).[79] As mentioned before in Scenario VII, the relatively high electronic conductivity in SCE facilitated the formation of Li clusters inside the SCE and then caused short circuits. With the introduction of $LiAlO_2$, the electronic conductivity was effectively reduced, resulting in outstanding cycling stability without short circuit. In addition, doping the SCE with other elements could achieve impressive properties. For some SCEs, effective doping enhanced the ionic conductivity and stability with Li. Zhang et al. reported an O-doped Li_6PS_5Br, in which the partial substitution of S with O comprehensively enhanced electrochemical properties including excellent dendrite suppression capability.[85]

Optimization of the Li Metal Anode

Dendrite growth often started from the interface between Li and SEs. For this reason, Li metal also highly affected dendrite growth. As already mentioned, the interface layer between Li and SE was significant for avoiding dendrites. In most ASLBs, Li foil was directly pressed onto the SE pallet to work as anode. However, this approach may cause voids and even gaps between Li and SE. Furthermore, Li foil had limited areal capacity and huge volume change, which may inhibit the power output. Novel design on the Li metal side thus represented another pathway to address the dendrite problem.

Temperature highly affects the properties of Li metal. Sakamoto's group has proved that the interface resistance between LLZO and Li dramatically decreases with a heating treatment at 175°C, which is lower than the melting point of Li (180°C).[42] Even though the interface resistance was decreased to 514 Ω cm^2, it was still

Please cite this article in press as: Cao et al., Lithium Dendrite in All-Solid-State Batteries: Growth Mechanisms, Suppression Strategies, and Characterizations, Matter (2020), https://doi.org/10.1016/j.matt.2020.03.015

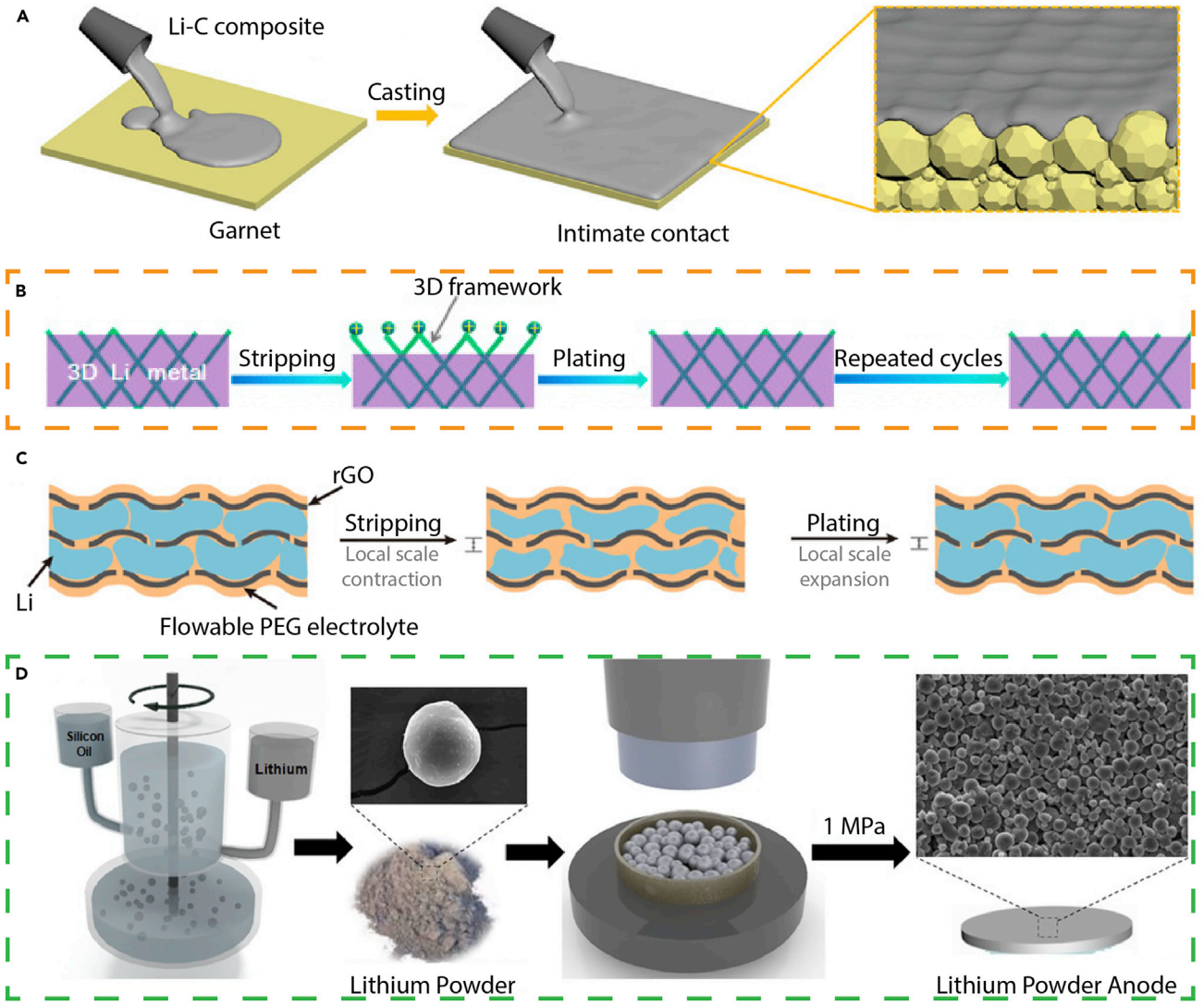

Figure 11. Dendrite Suppression through the Optimization of Li Metal

(A) Schematic showing the casting process of Li-graphite composites on garnet SCE and the obtained intimate contact. Adapted with permission from Duan et al.[87] Copyright 2019, Wiley-VCH Verlag GmbH & Co. KGaA, Weinheim.

(B) 3D Li metal. Schematic illustrating the plating and stripping process of Li on the 3D framework, where Li tends to nucleate and grow at the protuberances surface of 3D. Adapted with permission from Chi et al.[88] Copyright 2019, Elsevier Inc.

(C) Schematic illustrating the plating and stripping process whereby the interfacial fluctuation was reduced due to the increased Li surface area and flowable polymer electrolyte. Adapted with permission from Liu et al.[89] Copyright 2017, American Association for the Advancement of Science.

(D) Schematic illustrating the preparation process of Li powder via droplet emulsion technique and the corresponding SEM image. Adapted with permission from Shim et al.[90] Copyright 2017, Wiley-VCH Verlag GmbH & Co. KGaA, Weinheim.

much higher than that of OLEs-based LIB (in the tens of Ω cm^2), which could account for the poor contact between SE and Li foil. Based on these data, molten Li was selected to obtain a liquid-solid contact. However, the pallet had to be highly lithiumphilic and some SCEs were reported to drastically react with molten Li, which can lead to a dangerous thermal runaway.[86] To achieve a better wettability, Duan et al. fabricated a Li-graphite composite anode.[87] They mixed the graphite into molten Li to form a Li-C composite. This composite anode presented lower fluidity and higher viscosity compared with pure Li, which made it easy to be cast onto garnet to achieve an intimate contact (Figure 11A). In the mixing process, the

graphite was lithiated to LiC_6, which had lower reaction energy with garnet. As a result, the interface resistance was dramatically decreased to as low as 11 Ω cm^2 and stable cycling was achieved.

3D scaffolds have been widely applied in OLEs-based Li metal batteries to stabilize Li metal for their increased contact areas between Li and the electrolyte.[91–93] However, it is difficult to introduce rigid SCE into 3D structured Li, which made it more suitable to be applied in soft SPE. Chi et al. combined the 3D Li anode with a soft SPE interface to address the contact issue and dendrite formation in garnet-based ASLBs.[88] Li was infused into Ni foam to prepare a 3D Li. In their design, Li has the tendency to nucleate and grow at the protuberance surface of 3D frameworks, which formed uniform distribution of Li ions with increased deposition sites (Figure 11B). Meanwhile, the 3D structure decreased the effective current density. To achieve better interface contact between Li and electrolyte and further increase the areal capacity, Liu et al. incorporated the 3D Li and flowable polyethylene glycol (PEG) electrolyte into ASLBs.[89] With a thermal infusion approach, molten Li was infused into the well-stacking reduced graphene oxide (rGO) scaffold to prepare the layered Li-rGO electrode. Flowable PEG electrolyte was then infused into the 3D Li. Consequently, an intimate electrode-electrolyte contact was obtained because the flowable electrolyte adjusted its conformation during continuous plating and stripping, and the 3D Li dramatically decreased the local current density. Both of these factors contributed to the dendrite-free anode with high performance (Figure 11C).

Without a scaffold, fabricating Li with a larger surface area was another effective solution to suppress dendrites. Shim et al. prepared a Li powder-based anode using droplet emulsion technique followed by a compression procedure (Figure 11D).[90] After the compression, the Li powder maintained the spherical shape with average diameter of about 10 μm. Compared with Li foil, this Li powder-based anode exhibited larger surface area, which decreased the effective current density on each Li powder particle and eventually suppressed dendrite formation.

Introduction of Interface Buffer Layer

Interface stabilization was considered as an effective way to avoid dendrite formation. The reason for failure has been mooted with Scenario V. Inspired by the fact that SEI formed in OLEs has helped in stabilizing Li, introducing an interface buffer layer between Li and SE might also work.[94–97] According to its origin, the buffer layer was classified as a metastable interphase layer and an artificial interface layer. The metastable interphase layer was formed by the spontaneous reaction between Li and SEs when they made contact, while the artificial interface layer was an additional additive to stabilize the interface.

Metastable Interphase Layer

Li has high reactivity so that SEs can vigorously react with Li when they directly contact each other and form an interphase layer. This reaction consumes both SEs and Li. The property of the interphase layer largely affects the interface behavior. For example, even though LLZO is chemically resistant with Li, it has suffered from a severe dendrite problem. In contrast, dendrite growth can be prevented in $Li_{1+x}Al_xTi_{2-x}(PO_4)_3$ (LATP) due to the formation of SEI-like interphase layer.[98] However, the cells were terminated by substantially increased impedance at the interphase by its poor ionic conductivity. In another case, $Li_{1.4}Al_{0.4}Ge_{1.6}(PO_4)_3$ (LAGP) reacted with Li to form an interphase layer that exhibited a mixed ionic and electronic conductivity. Li was directly deposited at the interface between LAGP and the interphase layer, which led to the continuous decomposition of LAGP and

accelerated dendrite growth.[99] Therefore, the ideal interphase layer should be one with high ionic conductivity, electronic insulation, and high mechanical strength, all of which avoid the continuous reaction and dendrite formation.

Zhang et al. found that PVDF-LiN(SO_2F) (LiFSI)-based SPE had an open-circuit failure at high current density but with an atypical short circuit.[100] They attributed this dendrite-free phenomenon to the nanoscale interphase layer formed between Li and SPE, whose stable and uniform mosaic structure can suppress the Li dendrite growth. This interphase layer, i.e., LiF-sulfur compounds-LiOH-$LiCO_3$-Li_2O composite exhibited good ionic conductivity, electronic insulation, and high mechanical strength, which enabled good cycling performance and successful dendrite suppression (Figure 12A). In comparison, other PVDF-based interphase layers were composed of only few components and non-uniformly distributed. Even though they can still avoid dendrite formation, the cycling performance was poor. Other SCEs also had this metastable interphase layer to avoid dendrites. Li et al. introduced $LiZr_2(PO_4)_3$, which directly reacted with metallic Li anode to form a Li ion conductive passivation layer containing Li_3P and Li_8ZrO_6, where the interface wettability was optimized and dendrite formation was consequently suppressed.[101]

Inspired by the above research, additives that could form metastable interphase with Li were utilized to address the dendrite problem in some SCEs. Eshetu et al. designed a PEO-based electrolyte with Li azide (LiN_3) added to stabilize the Li metal.[102] As illustrated in Figure 12B, the LiN_3 reacted with Li to form highly ionic conductive Li_3N, which served as a robust SEI to protect Li. Meanwhile, the oxidation of LiN_3 at the cathode generated N_2, which migrated to the anode side and reacted with Li to form Li_3N. As a result, it showed no dendrite formation and long-term cycling. Han et al. introduced the addition of LiI into Li_2S-P_2S_5 glass, especially the 70(0.75Li_2S-0.25P_2S_5)-30LiI electrolyte, to effectively suppress dendrite formation and improve the CCD (Figure 12C).[103] The composition of SEI at the Li|electrolyte interface was tuned by the addition of LiI. In their previous work, they proved that the SEI composed of LiI or LiF can suppress dendrites due to high interface energy.[105] A similar strategy was applied in garnet-type electrolytes. With a melting-quenching method, Tian et al. introduced glassy-type Li_3OCl into $Li_{6.75}La_3Zr_{1.75}Ta_{0.25}O_{12}$ (LLZTO) electrolyte to address the dendrite growth issue (Figure 12D).[104] The amorphous Li_3OCl worked as a binder, filler, and bridge to fabricate an integrated composite electrolyte and continuous ionic conductivity network among LLZTO. More importantly, the *in situ* formed interphase layer, i.e., Li_2O and LiCl resulting from the reaction between Li_3OCl and Li, effectively suppressed dendrite growth in LLZTO.

Artificial Interface Layer

Not all the SEs had a proper metastable interphase layer with Li. A more universal and feasible strategy was to introduce an artificial interface layer between the SEs and Li to avoid the dendrite problem. Similarly to the metastable interphase layer, this artificial interface layer should have uniform coverage, good wettability with both Li and SEs, high ionic conductivity, poor electronic conductivity, and good mechanical strength. There have been many computationally predicted materials reported for artificial interface layers, such as Li salts-based organic-inorganic hybrid system, metal oxides, Li-based alloys, Li nitride, polymers, and ionic liquids. These materials were fabricated either on the Li metal side or on the SEs side.

The selection of this artificial interface layer was crucial for this strategy. The use of computational analysis has improved efficiency in the search for new materials.

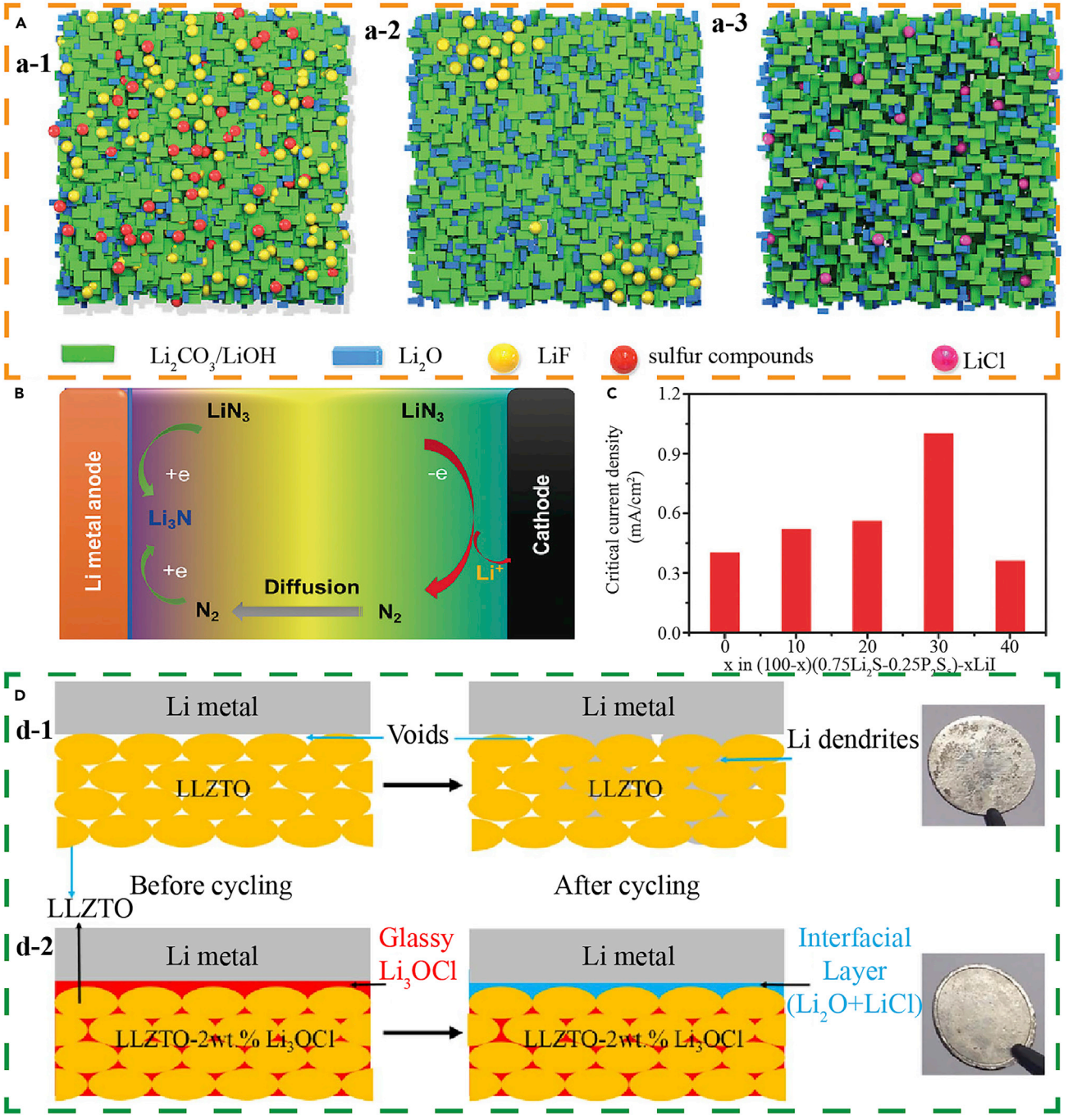

Figure 12. Metastable Interphase Layer Enabled Dendrite-Free Cycling

(A) Self-suppression of dendrite. Schematics illustrating the component distribution at PVDF-LiFSI|Li (a-1), PVDF-LiTFSI|Li (a-2), and PVDF-$LiClO_4$|Li (a-3) interfaces, which play important roles in dendrite suppression. Adapted with permission from Zhang et al.[100] Copyright 2019, Wiley-VCH Verlag GmbH & Co. KGaA, Weinheim.

(B–D) Additives with metastable interphase layer to improve the cycling behavior of the SPE, sulfide SCE, and oxide SCE. (B) Schematic illustrating the electrochemical reactions of LiN_3 and the formation of Li_3N to stabilize the interface between PEO-based electrolyte and Li metal. Adapted with permission from Eshetu et al.[102] Copyright 2017, Wiley-VCH Verlag GmbH & Co. KGaA, Weinheim. (C) The CCD of sulfide electrolyte varied according to the additive amount of LiI. Adapted with permission from Han et al.[103] Copyright 2018, Wiley-VCH Verlag GmbH & Co. KGaA, Weinheim. (D) Schematic illustrating dendrite growth in pure $Li_{6.75}La_3Zr_{1.75}Ta_{0.25}O_{12}$ (d-1) and dendrite suppression in $Li_{6.75}La_3Zr_{1.75}Ta_{0.25}O_{12}$ with 2 wt % Li_3OCl due to the formation of interphase layer with Li by the *in situ* reaction of Li_3OCl and Li metal (d-2). Adapted with permission from Tian et al.[104] Copyright 2018, Elsevier Inc.

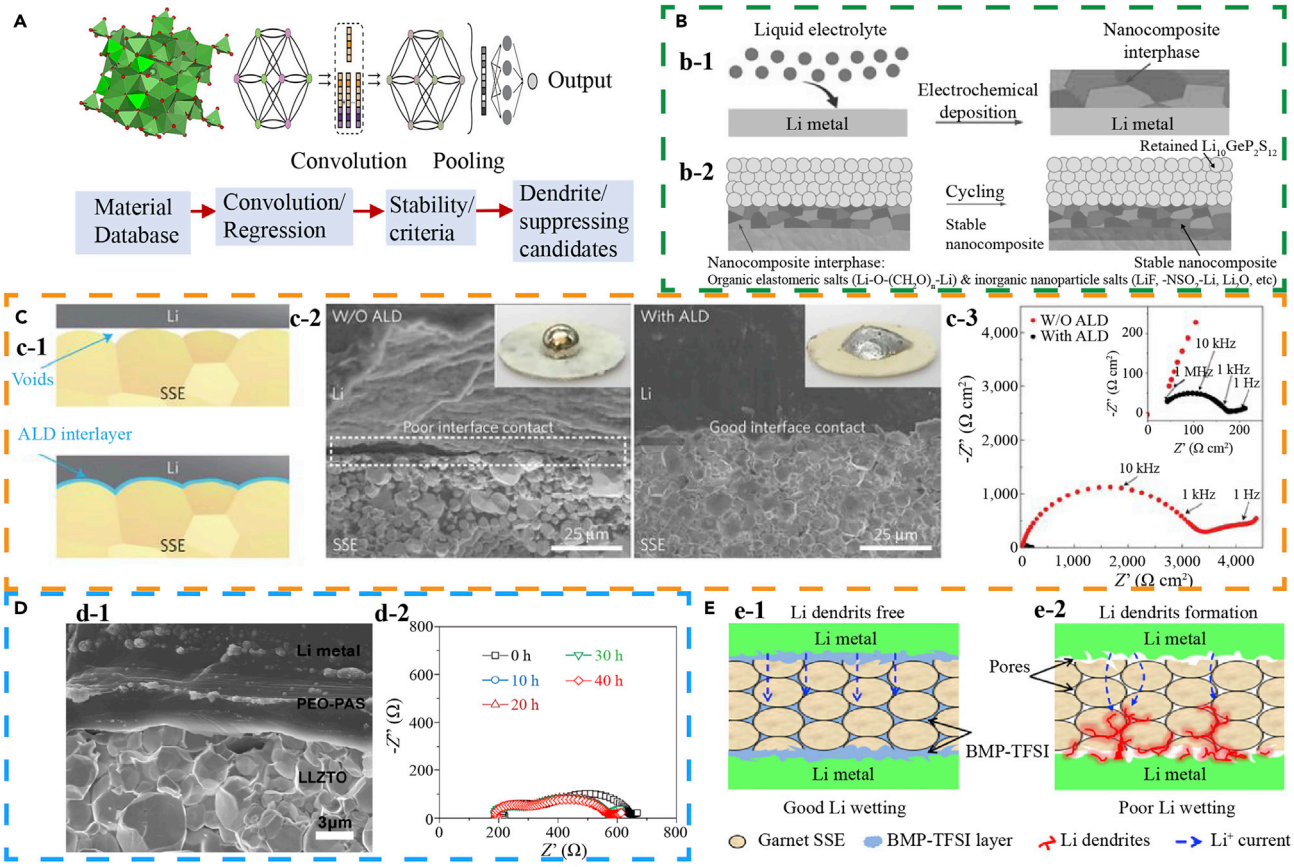

Figure 13. Introducing Artificial Interface Layer to Suppress Dendrite Growth

(A) Machine learning enabled computational screening of solid electrolytes with dendrite suppression. Adapted with permission from Ahmad et al.[106] Copyright 2018, American Chemical Society.

(B) Artificial SEI formed on the Li metal. Schematics illustrating the formation of nanocomposite interphase via electrochemical deposition in liquid electrolyte (b-1) and stabilized interface by the nanocomposite interphase consisting of organic elastomeric Li salts and inorganic nanoparticle salts (b-2). Adapted with permission from Gao et al.[108] Copyright 2018, Wiley-VCH Verlag GmbH & Co. KGaA, Weinheim.

(C) Interlayer enhanced wetting behavior of SCE with molten Li. (c-1) Schematic illustrating the intimate contact between SE and Li enabled by the ALD interlayer. (c-2) SEM images of interface between Li and SE with and without Al_2O_3 interlayer. (c-3) Comparison of EIS profiles revealing the dramatically reduced interface resistance. Adapted with permission from Han et al.[109] Copyright 2016, Springer Nature.

(D) Enhanced wettability and stability by introducing polymer at the interface between SCE and Li. (d-1) Cross-section SEM images of the Li|PEO-PAS|$Li_{6.5}La_3Zr_{1.5}Ta_{0.5}O_{12}$ showing the intimate contact. (d-2) Nyquist plots of the symmetric cell at different cycling times to show the stabilized interface. Adapted with permission from Zhou et al.[110] Copyright 2018, Elsevier Inc.

(E) Ionic liquid generated compact microstructure. Schematics illustrating dendrite-free cell due to the intimate contact and continuous Li^+ conducting network enabled by the ionic liquid (e-1) and dendrite formation caused by the poor Li wetting and concentrated Li^+ flux (e-2). Adapted with permission from Zhang et al.[111] Copyright 2018, Wiley-VCH Verlag GmbH & Co. KGaA, Weinheim.

Based on several criteria, novel materials can be screened out among over 10,000 materials in the database. Ahmad et al. performed a computational screening of over 12,000 electrolytes based on their properties for being mechanically isotropic and having anisotropic interfaces with Li metal, which were the two characteristics utilized as the criteria for dendrite suppression (Figure 13A).[106] To extend the data-set for screening, machine-learning models were chosen to predict the mechanical properties of materials to avoid the expensive first-principles calculation. As a result, they predicted over 20 mechanically anisotropic interfaces between Li metal and four solid electrolytes with the potential to suppress dendrite formation. Recently, Fitzhugh et al. also computationally evaluated the interface stability of $Li_{10}SiP_2S_{12}$ with over 67,000 materials, from which over 1,000 materials were predicted to

form stable interfaces for the anode range.[107] In their results, iodine-, phosphorus-, and nitrogen-based coating material had the highest performance in the 0- to 1.5-V range, which was consistent with other experimental results. Although the computational prediction still has some limitations in comprehensiveness for the electrolyte, the obtained results could guide the search for more promising electrolyte candidates.

Pretreatment of Li foil to form a stable SEI layer was an effective strategy to avoid dendrite formation. Gao et al. reported a novel approach to fabricate an interphase layer to stabilize the interface between Li and $Li_{10}GeP_2S_{12}$ (LGPS) via electrochemical decomposition of liquid electrolyte.[108] In their design, liquid electrolyte electrochemically decomposed and formed an interface layer on Li when applying a constant current (Figure 13B). The composition of this interface layer was adjustable by choosing different electrolytes and additives. As a result, the Li salt-based organic-inorganic nanocomposite insulated the LGPS and Li and had affinity for both of them in achieving a stable interface for dendrite-free cycling. With a similar strategy, Hou et al. fabricated an *ex situ* SEI on Li through electroplating precycled Li anode in an advanced electrolyte containing $LiNO_3$ and fluoroethylene carbonate (FEC). The robust SEI composed of LiF and Li_3N enabled a uniform and compact Li deposition, which effectively suppressed dendrite formation in LAGP.[112] The artificial SEI composed of inorganic-organic hybrid also suppressed dendrite formation as reported by Sun's group.[113] Molecular layer deposition (MLD) was utilized to coat Alucone on Li metal. This hybrid inorganic-organic SEI was demonstrated to have improved mechanical properties compared with pure inorganic coatings, and accommodated the stress and strain volume change that occurred during cycling.

Some oxide-based interface layers, such as Al_2O_3 and ZnO stabilized Li metal in OLEs, can be invoked to solve the dendrite issue in SEs. Wang et al. fabricated a conformal amorphous Al_2O_3 thin film on Li metal via magnetron sputtering techniques.[114] Since Al_2O_3 had low binding energy with Li, an ionic conductive Li-Al-O layer was formed at the interface. The authors found that Li plated homogeneously onto the Al_2O_3 surface, which was different from the generally accepted concept that Li plates were beneath the layer. Even though Li directly contacted SE, the amorphous and flat Li-Al-O layer induced a homogeneous Li nucleation in a layer-by-layer film-growth manner, which explained the highly stable and dendrite-free cycling. Zhong et al. introduced a Li-Al alloy layer onto Li *in situ* by pressing Al foil onto Li-boron alloy.[115] As a result, when matched with LAGP, the Li-Al alloy layer effectively avoided localized Li enrichment and suppressed dendrite formation.

Li metal has high reactivity with air, which hindered interface engineering on the Li metal side with methods such as atomic layer deposition (ALD) and the aforementioned MLD and sputtering. Introducing an artificial interlayer onto the SEs thus represented a feasible alternative to common interface engineering. Han et al. successfully addressed the wettability issue in garnet and Li by using an ultrathin Al_2O_3 layer by ALD (Figure 13C).[109] With the introduction of an Al_2O_3 layer, the voids between bare garnet and Li were avoided and intimate contact was achieved, and the interfacial impedance significantly decreased from 1,710 $\Omega\ cm^2$ to 1 $\Omega\ cm^2$. The lithiated Li-Al-O interface allowed effective Li ion transport and uniform Li deposition. In addition to Al_2O_3, Hu's group reported that Al, Si, and Ge coating layers between garnet and Li also effectively addressed the interface contact issue.[116–118] The alloys formed *in situ* such as Li-Al, Li-Si, and Li-Ge enabled highly decreased interface impedance and stable cycling.

The artificial interface layer should also have high ionic conductivity. Xu et al. replaced Li-blocking Li_2CO_3 with Li_3N on the surface of a garnet pellet, which possessed a high Li ion conductivity close to 10^{-3} S cm^{-1}.[119] To make a conformal coating, a thin Li layer was first evaporated onto an $Li_{6.5}La_3Zr_{1.5}Ta_{0.5}O_{12}$ pellet via electron beam thermal deposition system, then the Li_3N layer was prepared after filling with N_2. A highly ionic conductive Li_3N interface layer filled the energy gap between Li and SE, which enabled intimate contact between them and a significant decrease in interface resistance.

In comparison with inorganic ceramic materials, the soft property allowed the polymer to serve as a good interlayer to wet the interface between Li metal and SE and buffer the volume change of Li. Wang et al. reported that the modification of PEO on Li metal anode provided satisfactory mechanical property and intimate interface contact, which successfully suppressed dendrite formation.[120] However, due to the low Li^+ transference number of the polymer electrolyte, a strong electric field across the Li|polymer interface accelerated the Li dendrite nucleation (failure Scenario IV). To avoid this side effect, Zhou et al. coated the garnet surface with a thin polymer electrolyte with a transference number of 0.9 to address the dendrite issue in garnet electrolyte.[110] The single Li ion conducting polymer coating not only exhibited good adhesion to the SE and Li metal to achieve an intimate contact, but also insulated direct contact between Li metal and the grain boundaries of the SE, which delivered low and stable interface impedance (Figure 13D).

Non-flammable, intrinsic ionic conductive and viscous ionic liquids were widely studied as safe electrolytes in batteries, which were promising components in hybrid pseudo-solid electrolytes. Zhang et al. proposed an interfacial architecture engineered by incorporating an ionic liquid into the garnet-based structure to avoid dendrite formation (Figure 13E).[111] In their design, the voids were inside the SE with poor contact with Li, which were the main reason for dendrite growth. They later utilized soft and continuous ionic liquid to fill the voids and connect the grain boundaries. The coating layer formed a compact and stable interlayer between the Li metal and SE to resist the volume strain caused during cycling. Additionally, the continuous ionic liquid guided a uniform Li ion flux through the interface and avoided dendrite growth along the grain boundaries and voids inside the SE. In work by Wu's group, the introduction of viscoelastic and non-flammable ionic liquid at the interface between the Li metal and a composite polymer electrolyte suppressed dendrite growth.[121]

With the aforementioned strategies, dendrite growth in these cases was suppressed to some extent. To arrive at a clearer understanding, the growth mechanisms and corresponding suppression strategies are briefly summarized in Table 1. We assumed that dendrite growth is the only reason for the failure of ASLBs; meanwhile the strategies are mainly operated in lab-scale cells. There are numerous challenges hindering the commercialization of ASLBs, such as kinetic limitations at the interface.[74] The critical tasks for the commercialization of ASLBs include but are not limited to Li dendrite suppression. Other factors should also be considered and addressed.

CHARACTERIZATIONS OF LI METAL IN ASLBs

Characterization is significant in revealing the mechanisms of dendrite growth and developing novel strategies for suppressing dendrites in SEs. Unfortunately, it is still challenging to directly "see" how Li metal is formed and propagated. Li is undetectable in many conventional characterization approaches, such as energy-dispersive

Table 1. Brief Summary of Dendrite Growth Mechanisms and Corresponding Suppression Strategies

Solid Electrolytes	Dendrite Growth Mechanisms	Dendrite Suppression Strategies
Solid polymer electrolyte (SPE)	dendrite grows at the tip and penetrates the SPE through the soft part	• compositing polymer electrolyte with various additives (non-ion-conductive fillers and ion-conductive fillers) • employing Li metal with 3D structure • applying SPE with a self-generated interphase layer
	dendrite grows in lateral and extends from the side of the electrode and SPE	
	subsurface structure buried under dendritic structure triggers the formation of dendrite	• cleaning and flattening the surface for Li deposition • introducing artificial interface layer
	additional effect caused by the redistribution of charge in Li|SPE interface induces Li dendrite	• introducing an interlayer to block the movement of anion • applying single-ion transport polymer
Solid ceramic or glass electrolyte (SCE)	physical issues, such as the microstructure on the surface, void, and defect inside, and density of the SCE cause dendrite nucleation and growth	• fabricating pallet with higher density, fewer defects, smooth and impurity-free surface • introducing an artificial interface layer • optimizing Li metal
	grain boundaries induce Li propagation inside the SCE	• employing single-crystal SCE • fabricating pallet with higher density and fewer defects • compositing SCE with self-healing polymer
	electrons from the residual conductivity, oxygen framework, and pore surface induce the formation of Li cluster inside the SCE	• introducing interphase with low electronic conductivity at the grain boundaries • doping special elements
	enhanced electric field in the tips due to the highly stable chemical interface between SCE and Li triggers dendrite growth	• introducing an artificial interface layer on Li metal or SCE • applying SCE with self-generated interphase layer

X-ray spectroscopy (EDS), X-ray photoelectron spectroscopy (XPS), and X-ray diffraction (XRD). Moreover, opaque SEs further increase the difficulty for some approaches applied in OLEs, such as *in situ* observation of dendrite using an optical microscope. Electrochemical characterization is the most commonly applied approach to diagnose dendrite formation and short circuit of the cell, and the symmetric Li|SE|Li setup is employed to evaluate the cycling stability. However, researchers found that it is not convincing enough to characterize the dendrite issue only with the electrochemical approach; for example, the symmetrical cell can perform well even when the cell is short.[1] It is necessary to study dendrites in SEs with comprehensive characterization techniques.

In this section, we mainly introduce several effective techniques reported to observe the dendrite revolution and reveal the mechanism of dendrite growth. As shown in Figure 14, electrochemical characterization, SEM, optical microscopy, NDP, synchrotron X-ray tomography, and nuclear magnetic resonance (NMR) are introduced in detail, with the advantages (in green) and drawbacks (in blue) summarized.

Electrochemical Characterization

Galvanostatic cycling and EIS in a symmetric Li|SE|Li cell are conventional characterization approaches in the study of Li metal anode. The CCD value of SEs can be directly achieved based on the galvanostatic cycling result. The plating and

Please cite this article in press as: Cao et al., Lithium Dendrite in All-Solid-State Batteries: Growth Mechanisms, Suppression Strategies, and Characterizations, Matter (2020), https://doi.org/10.1016/j.matt.2020.03.015

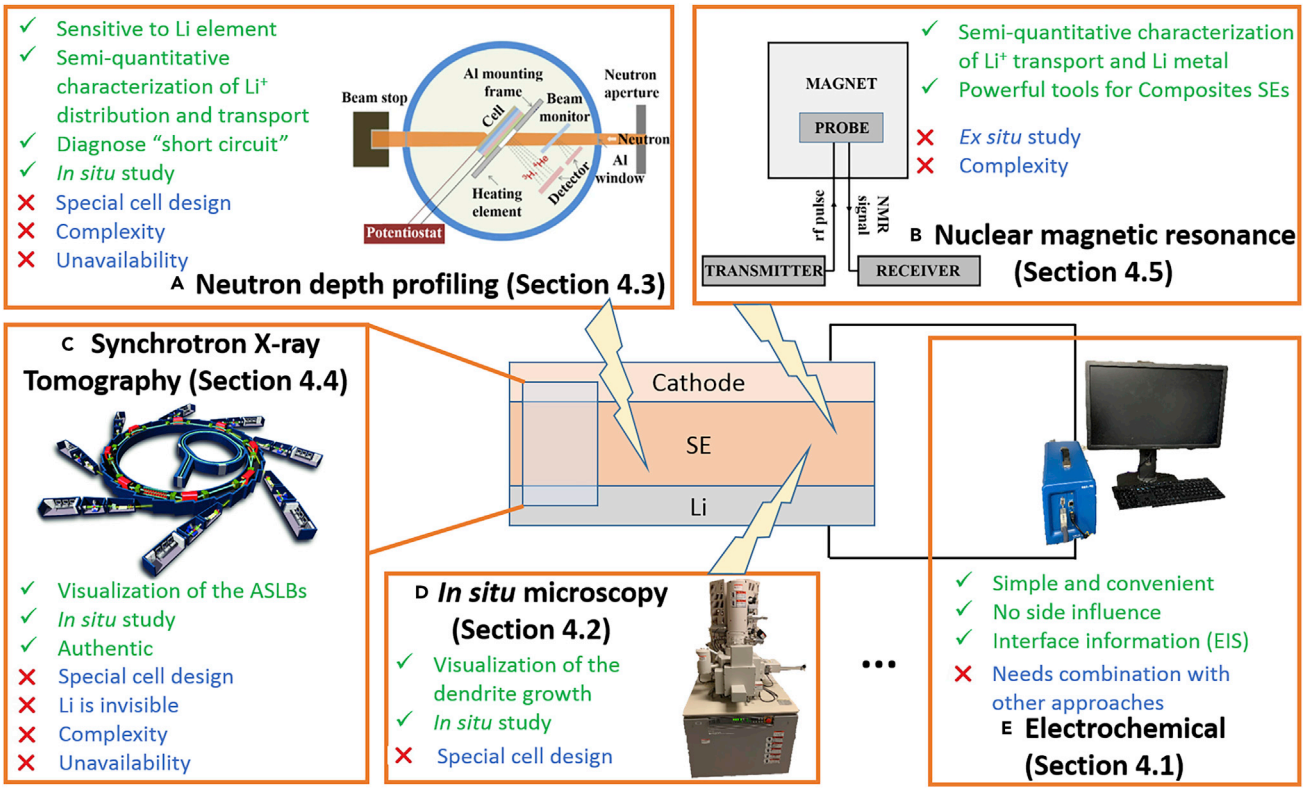

Figure 14. Characterization Techniques and Corresponding Advantages (in Green) and Shortages (in Blue) in the Study of Dendrite Growth in SEs.
(A) Neutron depth profiling. Adapted with permission from Han et al.[49] Copyright 2019, Springer Nature.
(B) Nuclear magnetic resonance.
(C) Synchrotron X-ray tomography. Copyright, Synchrotron SOLEIL/J.F. Santarelli.
(D) *In situ* microscopy.
(E) Electrochemical.

stripping voltage or overpotential can also reflect the interface information. In the other hand, EIS is a convenient technique without side influence that has been widely applied to investigate Li ion batteries. EIS can provide valuable information about the interfaces at electrode|SE and Li ion diffusion kinetics.

Figure 15A shows the polarization profiles of the symmetric cell at different current densities, where the abrupt drop of voltage to approximately 0 V indicates the short circuit due to dendrite growth.[42] As a result, the corresponding EIS before and after cycling characterizes this process. Before cycling, the symmetric cell exhibits a typical Nyquist plot, which consists of two semicircular features. The semicircle at high frequencies (7 MHz to 100 kHz) was attributed to the ohmic resistance of LLZO, and the one at low frequencies (100 kHz to 1 Hz) is consistent with charge-transfer resistance. In contrast, after cycling the Nyquist plot appeared at the fourth quadrant, which was consistent with an electronic short circuit exhibiting inductance.

It should be noted that, even if the cell has been in short, the cell voltage may not drop down to 0 V as the result of "hard short," which is defined as "soft short." Sometimes it is not easy to diagnose whether the cell is in "soft short," and the stable voltage profiles are regarded as a behavior of stabilized Li metal. As reported by

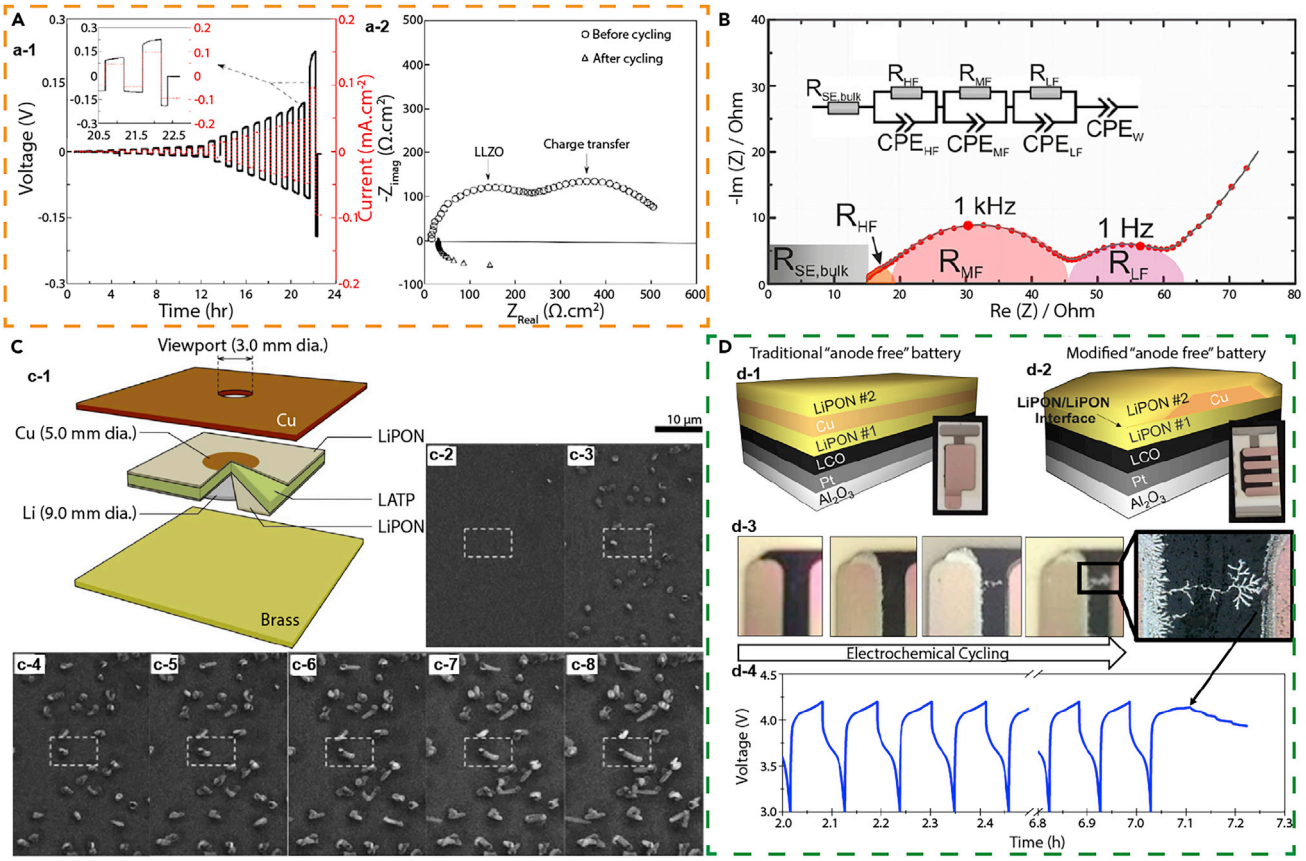

Figure 15. Electrochemical Impedance Spectroscopy and *In Situ* Observation via Scanning Electron Microscopy and Optical Microscopy

(A) Electrochemical studies of the symmetric cell via electrochemical impedance spectroscopy (EIS). (a-1) Galvanostatic cycling (the inset shows the last two cycles). (a-2) Nyquist plots before and after cycling Adapted with permission from Cheng et al.[42] Copyright 2017, Elsevier Inc..

(B) Nyquist plots for the all-solid-state full cell with $LiCoO_2$. Adapted with permission from Zhang et al.[122] Copyright 2017, American Chemical Society.

(C) *In situ* SEM observation of Li deposition in all-solid-state cell. (c-1) Specially designed all-solid electrochemical cell for *in situ* SEM observation. Sequential SEM images with intervals of 5 min during Li electrodeposition are shown in (c-2) to (c-8). Adapted with permission from Motoyama et al.[123] Copyright 2015, IOP Publishing Ltd.

(D) *In situ* observation of all-solid-state full cell through optical microscopy. Schematics of traditional Li-free battery (d-1) and modified "anode-free" Li ion battery with a LiPON-LiPON interface extending from the Cu current collector (d-2). (d-3) Photos of the Li deposition progress between two Cu electrodes. (d-4) Charge-discharge profiles of the full cell corresponding to the optical photos. Adapted with permission from Westover et al.[124] Copyright 2019, American Chemical Society.

Albertus et al., a limited Li amount (<30 um) can help identify the "soft short" by a full strip method, whereby the rise of potential when Li in one electrode was fully removed could prove the absence of "soft short."[1] Meanwhile, the measurement of activation energy for the electronic conductivity, EIS, and open-circuit voltage of the full cell are suggested to check for "soft short."

For the full cell, the EIS contained more information, including the interfacial processes in both anode and cathode. As shown in Figure 15B, Zhang et al. systematically studied the interfacial processes in ASLBs.[122] There were two obvious semicircles located in the mid-frequency region (1 kHz to 100 Hz) and low-frequency region (~1 Hz). At the high-frequency region (>1 MHz), the interception of 15 Ω represented the bulk resistance of the solid electrolyte ($R_{SE,bulk}$), which corresponds well with the thickness of roughly 590 μm and conductivity of 5 mS cm^{-1}. In addition, the small resistance (RHF ≈ 2 Ω) observed at around 518 kHz was attributed to the grain

boundary resistance in cold-pressed SE. The semicircle in the low-frequency region (RLF) was concluded to be the interface between the negative electrode and the SE. The semicircle in mid-frequency (R_{MF}) was assigned to the charge-transfer resistances and the electronic properties of the active material in cathode. The Warburg region was observed at very low frequency, which can be attributed to the Li^+ diffusion in cathode material.

In Situ Observation via Scanning Electron Microscopy and Optical Microscopy

Direct observation of the dendrite growth process inside the SE is essential for understanding dendrite formation and growth. Compared with the mostly applied *ex situ* investigation using SEM and optical microscopy, the *in situ* observation was more challenging due to high sensitivity of Li and invisibility of SEs. Therefore, special homemade cell designs and sample preparation were demanded for *in situ* observation of the dendrite growth process.

Figure 15C displays a cell design for *in situ* SEM experiments.[123] The $Li_{1+x+y}Al_xTi_{2-x}Si_yP_{3-y}O_{12}$ sheet was coated with a 2.5-μm-thick LiPON layer on both sides. Thereafter, Cu with thickness of 30–90 nm and diameter of 5 mm was deposited on the top of the LiPON to work as the current collector. The bottom of the LiPON was coated with a several-micrometer-thick Li film of diameter 9 mm. Finally, the layered structure was sandwiched by Cu and brass plates, with a viewport of diameter 3 mm in the center of the Cu plate. Under galvanostatic conditions, electrodeposition and dissolution of Li was performed and observed *in situ* through the viewport. As the deposition progressed, numerous small bumps with diameters of 1–2 μm gradually appeared and grew. The small bumps eventually broke the Cu layer and formed rods to penetrate the cracks.

Westover et al. designed a modified "anode-free" Li ion battery and observed branched tree-like structures of Li inside LiPON, as shown in Figure 15D.[124] The deposition of Li was observable because LiPON was optically transparent. Replacing the continuous Cu electrode in a traditional thin-film battery with footprint-type Cu current collector allowed the detection of the LiPON-LiPON interface between Cu. As the battery cycled, the Li layer extended as a branched tree-like morphology between two Cu electrodes. In the final cycle, a gradual drop in the voltage profile was observed. At this stage, one aggregate extended from the original Cu finger and touched the second Cu finger. The different state of charge caused the change in voltage profile.

Neutron Depth Profiling (NDP)

NDP, a non-destructive neutron analytical technique, is an advanced and powerful characterization approach to study batteries because of its high sensitivity to light elements. Specifically, it can quantitatively measure the Li distribution and observe *in situ* the dynamic evolution of Li concentration in LIBs. NDP thus represents an effective approach to study dendrite growth in SEs.

Wang et al. applied *in situ* NDP to monitor the Li plating-stripping behavior at garnet-electrode interfaces, as shown in Figure 16A[125] where the setup for *in situ* NDP is illustrated. As the neutron beam entered the chamber and reacted with the sample, ^3H and α particles were generated and detected by the Si detector. Extra heating at 90°C was applied to ensure that detectable amounts of Li transferred during short time spans. The cell structures were of the Li|garnet|Li symmetric and Li|garnet|carbon nanotube asymmetric types, whereby the *in situ* NDP provided

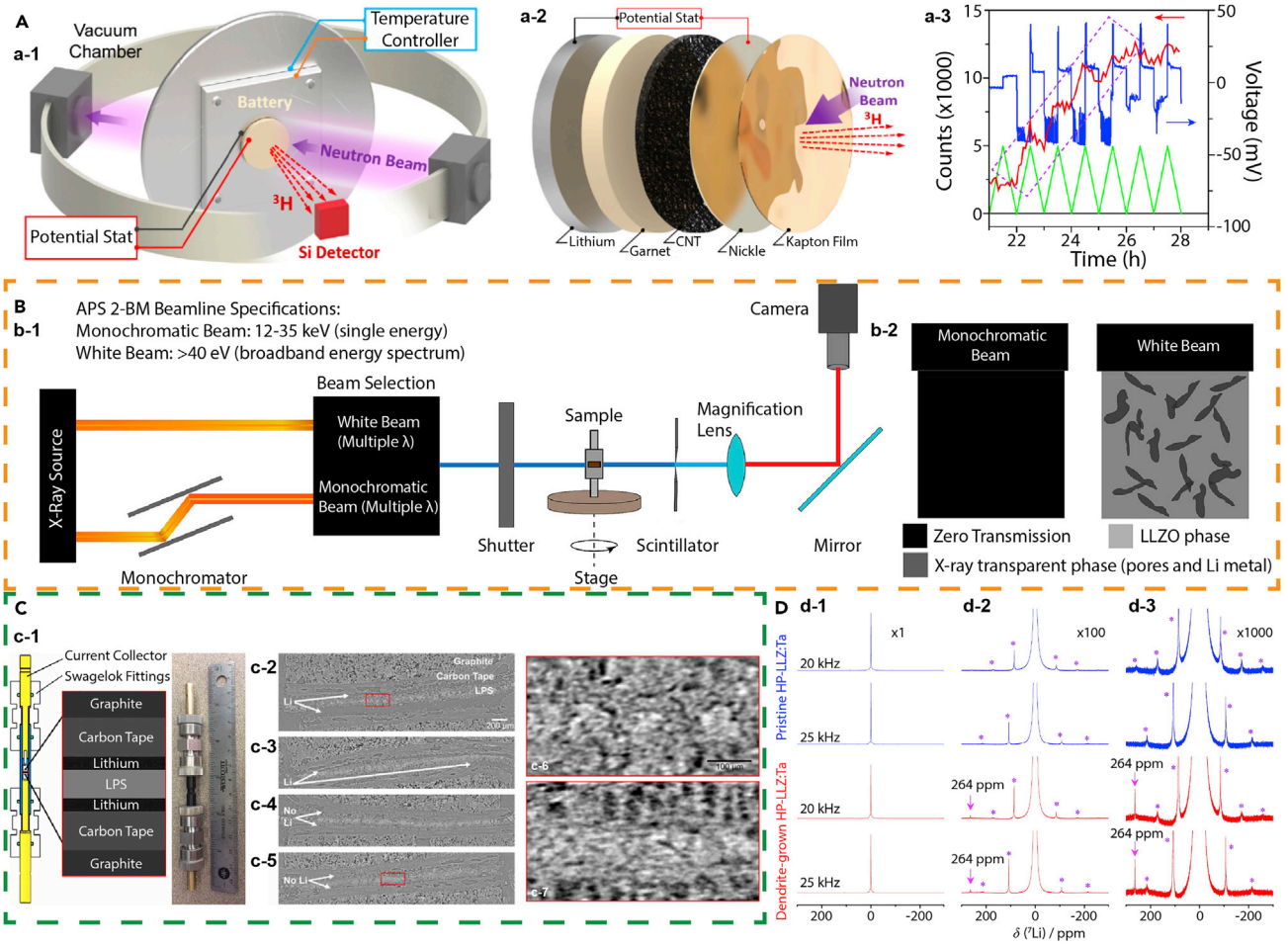

Figure 16. Neutron Depth Profiling, Synchrotron X-ray Tomography, and Nuclear Magnetic Resonance to Characterize the Evolution of Metallic Li Inside the SE

(A) *In situ* neutron depth profiling (NDP) measurement to monitor the Li plating and stripping behavior near electrode-electrolyte interface. Schematics illustrating the setup (a-1) and cell configuration (a-2) for NDP measurement. (a-3) Voltage profiles (blue), charge curve (green), and the integrated NDP count curve (red) of the symmetric cell at the "dynamic short circuit" stages Adapted with permission from Wang et al.[125] Copyright 2017, American Chemical Society..

(B) Synchrotron X-ray tomography for probing the evolution of submicron microstructure in dense SE during Li deposition. (b-1) Schematic of the synchrotron X-ray tomography setup. The beam energy and experiment setup are important. Images of garnet electrolytes show the attenuated X-rays under monochromatic beam (b-2) and well-identified pore phase and ceramic phase under high-energy white beam (b-3). Adapted with permission from Shen et al.[37] Copyright 2018, American Chemical Society.

(C) *In operando* X-ray tomography to three-dimensionally visualize Li anodes with SE. (c-1) Schematic and image of the cell for *in operando* observation through synchrotron X-ray tomography method. X-ray tomography reconstructions of Li|L_3PS_4|Li structures after 0 (c-2), 2 (c-3), and 5 (c-4) cycles. Zoomed view of the selected region in (c-2) and (c-4) are shown in (c-6) and (c-7), respectively. Adapted with permission from Seitzman et al.[126] Copyright 2018, IOP Publishing Ltd.

(D) ^{7}Li magic-angle spinning nuclear magnetic resonance spectra of pristine and dendrite-grown SE amplified 1-fold (d-1), 100-fold (d-2), and 1,000-fold (d-3). The signal at 264 ppm represents the existence of metallic Li. Adapted with permission from Tsai et al.[35] Copyright 2016, American Chemical Society.

abundant information on the Li ion transport behavior. In Li|garnet|Li cell, once the dendrite formed inside the garnet the NDP curve responded prior to the voltage profile. The accumulation of Li caused an increment in NDP counts, which well predicted dendrite growth and failure of the cell. With this technique, Han et al. reported the real-time visualization of Li dendrites in different SEs with *in operando* NDP to reveal the direct deposition of Li inside the SCE.[49]

Please cite this article in press as: Cao et al., Lithium Dendrite in All-Solid-State Batteries: Growth Mechanisms, Suppression Strategies, and Characterizations, Matter (2020), https://doi.org/10.1016/j.matt.2020.03.015

Synchrotron X-Ray Tomography

X-ray-based techniques such as EDS, XPS, and XRD have been widely applied in materials characterization. However, the light weight of Li makes it very difficult to apply these approaches to directly characterize Li with SEs. The most available techniques for imaging Li dendrites inside SEs are *ex situ* SEM and optical microscopy. Even with high-energy X-rays, it is difficult to achieve good phase contrast between metallic Li and SCEs.

Shen et al. applied synchrotron X-ray tomography to probe *in situ* the submicron microstructural change and track the failure mechanisms in SE.[37] The intensity of X-rays exponentially dropped after passing through a sample, where the beam energy and sample thickness greatly affected the transmission and image contrast. As shown in Figure 16B, synchrotron sources allowed a near-continuous selection of monochromatic beam energies and a polychromatic white beam with a broadband energy spectrum. The heavy Z-elements in thick LLZO blocked low-energy beams such as the 35-keV monochromatic beam. However, the beam with higher energy (>40 keV) distinguished the dense ceramic part (high attenuation coefficient) from the void and Li metal region (low attenuation coefficient). The polychromatic beam ensured good contrast between the SE and void (Li metal). In the meantime, Seitzman et al. designed an *in situ* sample holder to observe the microstructural evolution of Li_3PS_4 when matched with Li anode using high-resolution synchrotron X-ray sources (Figure 16C).[126] The cell was designed to avoid X-ray absorption by the sample holder and provided abundant *in operando* tomographic data. As the cell cycled, the apparent diminishing thickness of the Li foil was well revealed through the X-ray tomography reconstructions.

Nuclear Magnetic Resonance (NMR)

NMR is another powerful technique that can be used to identify metallic Li inside the SE. Tsai et al. applied ^{7}Li magic-angle spinning NMR to check the Li signals in Ta-substituted $Li_7La_3Zr_2O_{12}$ fabricated with hot pressing (HP-LLZ:Ta) before and after shorting, as shown in Figure 16D.[35] Obviously, all of the spectra showed a strong ^{7}Li signal located at a chemical shift of 0.6 ppm, which is attributed to the Li ions in SE. However, upon amplifying the spectra 1,000-fold, there is a ^{7}Li signal observed at 264 ppm in the dendrite-containing sample but not in the pristine sample. This high positive shift for ^{7}Li showed the presence of metallic Li, which verified the presence of dendrites inside the SE. Zheng et al. also applied high-resolution solid-state Li NMR to investigate Li ion transport behavior in an SCE.[127] By comparing the ^{6}Li spectra of the SCE before and after cycling, different Li ion-diffusion pathways were proposed and studied.

SUMMARY AND OUTLOOK

Driven by the increasing demand for energy worldwide, the goal of this review is to summarize dendrite growth in Li metal anodes in solid-state batteries to achieve higher-energy, higher-power, safer, and more reliable batteries. Li dendrite formation mechanisms in polymer and inorganic solid ceramic or glass electrolytes were systematically summarized, and Li dendrite suppression strategies and characterization of the Li metal anode were discussed in depth. In solid-state batteries, Li dendrites can grow for various reasons including the uneven contact between the electrolyte and Li metal interface, defects, grain boundaries, voids within the electrolyte, space charge, and electrical conductivity of the electrolyte. Correspondingly, the interface stabilization layers, structural design of anode and electrolyte, and chemical modification of the electrolyte and anode have been employed to stabilize the Li

metal. Furthermore, *ex situ*, *in situ*, and *in operando* methods, such as EIS, SEM, optical microscopy, synchrotron X-ray tomography, NDP, and NMR have been used to characterize the metal anode. This review thus represents a timely and important guide for the development and commercialization of safe and high-energy-density solid-state batteries.

For the future, there are other significant challenges to address in order to use Li metal as an anode in all-solid-state batteries. Here we make some suggestions solely for the study of Li metal when matching with SEs. (1) Standard Coulombic efficiency characterization, more powerful *in situ* characterization techniques, a limited amount of Li, identification of "soft short" at an early stage, and thinner electrolyte are suggested for the evaluation of dendrite suppression. (2) Current Li metal protection approaches are mostly tested at present within coin cells. It is of practical importance to test the Li metal stabilization in a larger cell, such as a pouch cell. (3) A stable and functional artificial interphase layer between SE and Li metal is critical. (4) Computational simulation plays an increasingly significant role in searching for novel electrolyte candidates, assisting the experimenter to obtain deeper understanding and prediction of performance. A fundamental understanding at multiple scales through computation, especially with interface layers, can guide improvements in Li metal anode design and interface stabilization, and eventually lead to the commercial manufacture of Li metal anodes in ASLBs.

Even though the solid-state electrolyte has not addressed the dendrite issue as successfully as expected thus far, all of the studies mentioned herein can lead to deeper understanding and provide strategies to stabilize the Li metal anode. The combination of Li metal anode and solid-state electrolyte remains a potential strategy to achieve a safe, high-performance, and low-cost energy-storage system in the future. At present, among the various aforementioned strategies, compositing ceramic or glass electrolyte with polymer hybrid and introducing an artificial interface stabilization layer between Li and electrolyte are the mostly common and promising methods. In the future, the mechanisms of dendrite growth in SEs need to be further investigated and understood before more practical and scalable strategies can pave the new paths to address the dendrite issue.

ACKNOWLEDGMENTS

H.Z. acknowledges financial support from the program of electrochemical systems in the division of chemical, bioengineering, environmental and transport systems in the National Science Foundation (award number: 1924534) and Rogers Corporation, United States.

AUTHOR CONTRIBUTIONS

Conceptualization, H.Z.; Visualization, D.C., X.S., and H.Z.; Writing – Original Draft, D.C., X.S., and H.Z.; Writing – Review & Editing, D.C., X.S., Q.L., A.N., P.X., and H.Z.; Copyright, P.X.; Funding Acquisition, H.Z.; Supervision, H.Z.

REFERENCES

1. Albertus, P., Babinec, S., Litzelman, S., and Newman, A. (2018). Status and challenges in enabling the lithium metal electrode for high-energy and low-cost rechargeable batteries. Nat. Energy. *3*, 16–21.

2. Palacín, M.R., and de Guibert, A. (2016). Why do batteries fail? Science *351*, 1253292.

3. Choi, J.W., and Aurbach, D. (2016). Promise and reality of post-lithium-ion batteries with high energy densities. Nat. Rev. Mater. *1*, 16013.

4. Armand, M., and Tarascon, J.M. (2008). Building better batteries. Nature *451*, 652.

5. Placke, T., Kloepsch, R., Dühnen, S., and Winter, M. (2017). Lithium ion, lithium metal, and alternative rechargeable battery technologies: the odyssey for high energy density. J. Solid State Electrochem. *21*, 1939–1964.

6. Schmuch, R., Wagner, R., Hörpel, G., Placke, T., and Winter, M. (2018). Performance and cost of materials for lithium-based

rechargeable automotive batteries. Nat. Energy. *3*, 267–278.

7. Cheng, X.-B., Zhang, R., Zhao, C.-Z., and Zhang, Q. (2017). Toward safe lithium metal anode in rechargeable batteries: a review. Chem. Rev. *117*, 10403–10473.

8. Yamada, Y., and Yamada, A. (2015). Review—superconcentrated electrolytes for lithium batteries. J. Electrochem. Soc. *162*, A2406–A2423.

9. Ding, F., Xu, W., Graff, G.L., Zhang, J., Sushko, M.L., Chen, X., Shao, Y., Engelhard, M.H., Nie, Z., Xiao, J., et al. (2013). Dendrite-free lithium deposition via self-healing electrostatic shield mechanism. J. Am. Chem. Soc. *135*, 4450–4456.

10. Li, N.-W., Yin, Y.-X., Yang, C.-P., and Guo, Y.-G. (2016). An artificial solid electrolyte interphase layer for stable lithium metal anodes. Adv. Mater. *28*, 1853–1858.

11. Tantratian, K., Cao, D., Abdelaziz, A., Sun, X., Sheng, J., Natan, A., Chen, L., and Zhu, H. (2020). Stable Li metal anode enabled by space confinement and uniform curvature through lithiophilic nanotube Arrays. Adv. Energy Mater. *10*, 1902819.

12. Monroe, C., and Newman, J. (2005). The impact of elastic deformation on deposition kinetics at lithium/polymer interfaces. J. Electrochem. Soc. *152*, A396–A404.

13. Wolfenstine, J., Allen, J.L., Sakamoto, J., Siegel, D.J., and Choe, H. (2018). Mechanical behavior of Li-ion-conducting crystalline oxide-based solid electrolytes: a brief review. Ionics *24*, 1271–1276.

14. Ni, J.E., Case, E.D., Sakamoto, J.S., Rangasamy, E., and Wolfenstine, J.B. (2012). Room temperature elastic moduli and Vickers hardness of hot-pressed LLZO cubic garnet. J. Mater. Sci. *47*, 7978–7985.

15. Baranowski, L.L., Heveran, C.M., Ferguson, V.L., and Stoldt, C.R. (2016). Multi-scale mechanical behavior of the Li_3PS_4 solid-phase electrolyte. ACS Appl. Mater. Interfaces *8*, 29573–29579.

16. Zeng, X.-X., Yin, Y.-X., Li, N.-W., Du, W.-C., Guo, Y.-G., and Wan, L.-J. (2016). Reshaping lithium plating/stripping behavior via bifunctional polymer electrolyte for room-temperature solid Li metal batteries. J. Am. Chem. Soc. *138*, 15825–15828.

17. Dolle, M., Sannier, L., Beaudoin, B., Trentin, M., and Tarascon, J.M. (2002). Live scanning electron microscope observations of dendritic growth in lithium/polymer cells. Electrochem. Solid St. *5*, A286–A289.

18. Khurana, R., Schaefer, J.L., Archer, L.A., and Coates, G.W. (2014). Suppression of lithium dendrite growth using cross-linked polyethylene/poly(ethylene oxide) electrolytes: a new approach for practical lithium-metal polymer batteries. J. Am. Chem. Soc. *136*, 7395–7402.

19. Cheng, X.-B., Zhao, C.-Z., Yao, Y.-X., Liu, H., and Zhang, Q. (2019). Recent advances in energy Chemistry between solid-state electrolyte and safe lithium-metal anodes. Chem *5*, 74–96.

20. Yang, C., Fu, K., Zhang, Y., Hitz, E., and Hu, L. (2017). Protected lithium-metal anodes in batteries: from liquid to solid. Adv. Mater. *29*, 1701169.

21. Fan, L., Wei, S., Li, S., Li, Q., and Lu, Y. (2018). Recent progress of the solid-state electrolytes for high-energy metal-based batteries. Adv. Energy Mater. *8*, 1702657.

22. Wan, J., Xie, J., Mackanic, D.G., Burke, W., Bao, Z., and Cui, Y. (2018). Status, promises, and challenges of nanocomposite solid-state electrolytes for safe and high performance lithium batteries. Mater. Today Nano. *4*, 1–16.

23. Barton, J.L., Bockris, J.O., Apos, M., and Ubbelohde Alfred Rene Jean, P. (1962). The electrolytic growth of dendrites from ionic solutions. Proc. Roy. Soc. Lond. Math. Phys. Sci. *268*, 485–505.

24. Brissot, C., Rosso, M., Chazalviel, J.N., and Lascaud, S. (1999). Dendritic growth mechanisms in lithium/polymer cells. J. Power Sourc. *81-82*, 925–929.

25. Monroe, C., and Newman, J. (2003). Dendrite growth in lithium/polymer systems: a propagation model for liquid electrolytes under galvanostatic conditions. J. Electrochem. Soc. *150*, A1377–A1384.

26. Harry, K.J., Hallinan, D.T., Parkinson, D.Y., MacDowell, A.A., and Balsara, N.P. (2013). Detection of subsurface structures underneath dendrites formed on cycled lithium metal electrodes. Nat. Mater. *13*, 69.

27. Zhou, W., Wang, S., Li, Y., Xin, S., Manthiram, A., and Goodenough, J.B. (2016). Plating a dendrite-free lithium anode with a polymer/ceramic/polymer sandwich electrolyte. J. Am. Chem. Soc. *138*, 9385–9388.

28. Cao, C., Li, Y., Feng, Y., Peng, C., Li, Z., and Feng, W. (2019). A solid-state single-ion polymer electrolyte with ultrahigh ionic conductivity for dendrite-free lithium metal batteries. Energy Storage Mater *19*, 401–407.

29. Zhao, C.-Z., Chen, P.-Y., Zhang, R., Chen, X., Li, B.-Q., Zhang, X.-Q., Cheng, X.-B., and Zhang, Q. (2018). An ion redistributor for dendrite-free lithium metal anodes. Sci. Adv. *4*, eaat3446.

30. Chazalviel, J.N. (1990). Electrochemical aspects of the generation of ramified metallic electrodeposits. Phy. Rev. A *42*, 7355–7367.

31. Maier, J. (1995). Ionic conduction in space charge regions. Prog. Solid State Chem. *23*, 171–263.

32. Shen, Y., Zhang, Y., Han, S., Wang, J., Peng, Z., and Chen, L. (2018). Unlocking the energy capabilities of lithium metal electrode with solid-state electrolytes. Joule *2*, 1674–1689.

33. Brogioli, D., Langer, F., Kun, R., and La Mantia, F. (2019). Space-charge effects at the $Li_7La_3Zr_2O_{12}$/Poly(ethylene oxide) interface. ACS Appl. Matter. Interfaces *11*, 11999–12007.

34. Long, L., Wang, S., Xiao, M., and Meng, Y. (2016). Polymer electrolytes for lithium polymer batteries. J. Mater. Chem. A *4*, 10038–10069.

35. Tsai, C.-L., Roddatis, V., Chandran, C.V., Ma, Q., Uhlenbruck, S., Bram, M., Heitjans, P., and Guillon, O. (2016). $Li_7La_3Zr_2O_{12}$ interface modification for Li dendrite prevention. ACS Appl. Mater. Interfaces *8*, 10617–10626.

36. Wu, J.-F., Pu, B.-W., Wang, D., Shi, S.-Q., Zhao, N., Guo, X., and Guo, X. (2019). In situ formed shields enabling Li_2CO_3-free solid electrolytes: a new route to uncover the intrinsic lithiophilicity of garnet electrolytes for dendrite-free Li-metal batteries. ACS Appl. Mater. Interfaces *11*, 898–905.

37. Shen, F., Dixit, M.B., Xiao, X., and Hatzell, K.B. (2018). Effect of pore connectivity on Li dendrite propagation within LLZO electrolytes observed with synchrotron X-ray tomography. ACS Energy Lett. *3*, 1056–1061.

38. Porz, L., Swamy, T., Sheldon, B.W., Rettenwander, D., Frömling, T., Thaman, H.L., Berendts, S., Uecker, R., Carter, W.C., and Chiang, Y.-M. (2017). Mechanism of lithium metal penetration through inorganic solid electrolytes. Adv. Energy Mater. *7*, 1701003.

39. Kataoka, K., Nagata, H., and Akimoto, J. (2018). Lithium-ion conducting oxide single crystal as solid electrolyte for advanced lithium battery application. Sci. Rep. *8*, 9965.

40. Li, Y., Wang, Z., Li, C., Cao, Y., and Guo, X. (2014). Densification and ionic-conduction improvement of lithium garnet solid electrolytes by flowing oxygen sintering. J. Power Sources *248*, 642–646.

41. Nagao, M., Hayashi, A., Tatsumisago, M., Kanetsuku, T., Tsuda, T., and Kuwabata, S. (2013). In situ SEM study of a lithium deposition and dissolution mechanism in a bulk-type solid-state cell with a Li_2S-P_2S_5 solid electrolyte. Phys. Chem. Chem. Phys. *15*, 18600–18606.

42. Cheng, E.J., Sharafi, A., and Sakamoto, J. (2017). Intergranular Li metal propagation through polycrystalline $Li_{6.25}Al_{0.25}La_3Zr_2O_{12}$ ceramic electrolyte. Electrochim. Acta *223*, 85–91.

43. Yu, S., and Siegel, D.J. (2017). Grain boundary contributions to Li-ion transport in the solid electrolyte $Li_7La_3Zr_2O_{12}$ (LLZO). Chem. Mater. *29*, 9639–9647.

44. Yu, S., and Siegel, D.J. (2018). Grain boundary softening: a potential mechanism for lithium metal penetration through stiff solid electrolytes. ACS Appl. Mater. Interfaces *10*, 38151–38158.

45. Pesci, F.M., Brugge, R.H., Hekselman, A.K.O., Cavallaro, A., Chater, R.J., and Aguadero, A. (2018). Elucidating the role of dopants in the critical current density for dendrite formation in garnet electrolytes. J. Mater. Chem. A *6*, 19817–19827.

46. Cheng, L., Chen, W., Kunz, M., Persson, K., Tamura, N., Chen, G., and Doeff, M. (2015). Effect of surface microstructure on electrochemical performance of garnet solid electrolytes. ACS Appl. Mater. Interfaces *7*, 2073–2081.

47. Raj, R., and Wolfenstine, J. (2017). Current limit diagrams for dendrite formation in solid-state electrolytes for Li-ion batteries. J. Power Sources *343*, 119–126.

48. Ishiguro, K., Nemori, H., Sunahiro, S., Nakata, Y., Sudo, R., Matsui, M., Takeda, Y., Yamamoto, O., and Imanishi, N. (2014). Ta-doped $Li_7La_3Zr_2O_{12}$ for water-stable lithium electrode of lithium-air batteries. J. Electrochem. Soc. *161*, A668–A674.

49. Han, F., Westover, A.S., Yue, J., Fan, X., Wang, F., Chi, M., Leonard, D.N., Dudney, N.J., Wang, H., and Wang, C. (2019). High electronic conductivity as the origin of lithium dendrite formation within solid electrolytes. Nat. Energy *4*, 187–196.

50. Chen, Y.-T., Jena, A., Pang, W.K., Peterson, V.K., Sheu, H.-S., Chang, H., and Liu, R.-S. (2017). Voltammetric enhancement of Li-ion conduction in Al-doped $Li_{7-x}La_3Zr_2O_{12}$ solid electrolyte. J. Phy. Chem. C *121*, 15565–15573.

51. Aguesse, F., Manalastas, W., Buannic, L., Lopez del Amo, J.M., Singh, G., Llordés, A., and Kilner, J. (2017). Investigating the dendritic growth during full cell cycling of garnet electrolyte in direct contact with Li metal. ACS Appl. Mater. Interfaces *9*, 3808–3816.

52. Tian, H.-K., Xu, B., and Qi, Y. (2018). Computational study of lithium nucleation tendency in $Li_7La_3Zr_2O_{12}$ (LLZO) and rational design of interlayer materials to prevent lithium dendrites. J. Power Sources *392*, 79–86.

53. Wang, S., Xu, H., Li, W., Dolocan, A., and Manthiram, A. (2018). Interfacial chemistry in solid-state batteries: formation of interphase and its consequences. J. Am. Chem. Soc. *140*, 250–257.

54. Gurevitch, I., Buonsanti, R., Teran, A.A., Gludovatz, B., Ritchie, R.O., Cabana, J., and Balsara, N.P. (2013). Nanocomposites of titanium dioxide and polystyrene-poly(ethylene oxide) block copolymer as solid-state electrolytes for lithium metal batteries. J. Electrochem. Soc. *160*, A1611–A1617.

55. Huo, H., Chen, Y., Luo, J., Yang, X., Guo, X., and Sun, X. (2019). Rational design of hierarchical "ceramic-in-polymer" and "polymer-in-ceramic" electrolytes for dendrite-free solid-state batteries. Adv. Energy Mater. *9*, 1804004.

56. Wang, X., Zhang, Y., Zhang, X., Liu, T., Lin, Y.-H., Li, L., Shen, Y., and Nan, C.-W. (2018). Lithium-salt-rich PEO/$Li_{0.3}La_{0.557}TiO_3$ interpenetrating composite electrolyte with three-dimensional ceramic nano-backbone for all-solid-state lithium-ion batteries. ACS Appl. Mater. Interfaces *10*, 24791–24798.

57. Li, D., Chen, L., Wang, T., and Fan, L.-Z. (2018). 3D fiber-network-reinforced bicontinuous composite solid electrolyte for dendrite-free lithium metal batteries. ACS Appl. Mater. Interfaces *10*, 7069–7078.

58. Tang, W., Tang, S., Zhang, C., Ma, Q., Xiang, Q., Yang, Y.-W., and Luo, J. (2018). Simultaneously enhancing the thermal stability, mechanical modulus, and electrochemical performance of solid polymer electrolytes by incorporating 2D sheets. Adv. Energy Mater. *8*, 1800866.

59. Lin, D., Yuen, P.Y., Liu, Y., Liu, W., Liu, N., Dauskardt, R.H., and Cui, Y. (2018). A silica-aerogel-reinforced composite polymer electrolyte with high ionic conductivity and high modulus. Adv. Mater. *30*, 1802661.

60. Lin, D., Liu, W., Liu, Y., Lee, H.R., Hsu, P.-C., Liu, K., and Cui, Y. (2016). High ionic conductivity of composite solid polymer electrolyte via in situ synthesis of monodispersed SiO2 nanospheres in poly(ethylene oxide). Nano Lett. *16*, 459–465.

61. Choudhury, S., Mangal, R., Agrawal, A., and Archer, L.A. (2015). A highly reversible room-temperature lithium metal battery based on crosslinked hairy nanoparticles. Nat. Commun. *6*, 10101.

62. Zhang, X., Xie, J., Shi, F., Lin, D., Liu, Y., Liu, W., Pei, A., Gong, Y., Wang, H., Liu, K., et al. (2018). Vertically aligned and continuous nanoscale ceramic–polymer interfaces in composite solid polymer electrolytes for enhanced ionic conductivity. Nano Lett. *18*, 3829–3838.

63. Xia, Q., Wu, J., Shi, Q.X., Xiang, X., Li, X., Pei, H., Zeng, H., Xie, X., and Ye, Y.S. (2019). UV-curable boron nitride nanosheet/ionic liquid-based crosslinked composite polymer electrolyte in lithium metal batteries. J. Power Sources *414*, 283–292.

64. Yang, L., Wang, Z., Feng, Y., Tan, R., Zuo, Y., Gao, R., Zhao, Y., Han, L., Wang, Z., and Pan, F. (2017). Flexible composite solid electrolyte facilitating highly stable "soft contacting" Li–electrolyte interface for solid state lithium-ion batteries. Adv. Energy Mater. *7*, 1701437.

65. Guo, Q., Han, Y., Wang, H., Xiong, S., Sun, W., Zheng, C., and Xie, K. (2019). Novel synergistic coupling composite chelating copolymer/LAGP solid electrolyte with optimized interface for dendrite-free solid Li-metal battery. Electrochim. Acta *296*, 693–700.

66. Zhang, J., Zang, X., Wen, H., Dong, T., Chai, J., Li, Y., Chen, B., Zhao, J., Dong, S., Ma, J., et al. (2017). High-voltage and free-standing poly(propylene carbonate)/$Li_{6.75}La_3Zr_{1.75}Ta_{0.25}O_{12}$ composite solid electrolyte for wide temperature range and flexible solid lithium ion battery. J. Mater. Chem. A *5*, 4940–4948.

67. Zhang, J., Zhao, N., Zhang, M., Li, Y., Chu, P.K., Guo, X., Di, Z., Wang, X., and Li, H. (2016). Flexible and ion-conducting membrane electrolytes for solid-state lithium batteries: dispersion of garnet nanoparticles in insulating polyethylene oxide. Nano Energy *28*, 447–454.

68. Yang, C., Liu, B., Jiang, F., Zhang, Y., Xie, H., Hitz, E., and Hu, L. (2017). Garnet/polymer hybrid ion-conducting protective layer for stable lithium metal anode. Nano Res. *10*, 4256–4265.

69. Chen, L., Li, Y., Li, S.-P., Fan, L.-Z., Nan, C.-W., and Goodenough, J.B. (2018). PEO/garnet composite electrolytes for solid-state lithium batteries: from "ceramic-in-polymer" to "polymer-in-ceramic". Nano Energy *46*, 176–184.

70. Zhao, C.-Z., Zhang, X.-Q., Cheng, X.-B., Zhang, R., Xu, R., Chen, P.-Y., Peng, H.-J., Huang, J.-Q., and Zhang, Q. (2017). An anion-immobilized composite electrolyte for dendrite-free lithium metal anodes. Proc. Natl. Acad. Sci. U S A *114*, 11069–11074.

71. Whiteley, J.M., Hafner, S., Zhu, C., Zhang, W., and Lee, S.-H. (2017). Stable lithium deposition using a self-optimizing solid electrolyte composite. J. Electrochem. Soc. *164*, A2962–A2966.

72. Lu, Y., Tikekar, M., Mohanty, R., Hendrickson, K., Ma, L., and Archer, L.A. (2015). Stable cycling of lithium metal batteries using high transference number electrolytes. Adv. Energy Mater. *5*, 1402073.

73. Chen, L., Li, W., Fan, L.-Z., Nan, C.-W., and Zhang, Q. (2019). Intercalated electrolyte with high transference number for dendrite-free solid-state lithium batteries. Adv. Funct. Mater. *29*, 1901047.

74. Kerman, K., Luntz, A., Viswanathan, V., Chiang, Y.-M., and Chen, Z. (2017). Review—practical challenges hindering the development of solid state Li ion batteries. J. Electrochem. Soc. *164*, A1731–A1744.

75. Yi, E., Wang, W., Kieffer, J., and Laine, R.M. (2016). Flame made nanoparticles permit processing of dense, flexible, Li+ conducting ceramic electrolyte thin films of cubic-$Li_7La_3Zr_2O_{12}$ (c-LLZO). J. Mater. Chem. A *4*, 12947–12954.

76. Xu, S., McOwen, D.W., Zhang, L., Hitz, G.T., Wang, C., Ma, Z., Chen, C., Luo, W., Dai, J., Kuang, Y., et al. (2018). All-in-one lithium-sulfur battery enabled by a porous-dense-porous garnet architecture. Energy Storage Mater *15*, 458–464.

77. Thomas-Alyea, K.E. (2018). Design of porous solid electrolytes for rechargeable metal batteries. J. Electrochem. Soc. *165*, A1523–A1528.

78. Li, Y., Chen, X., Dolocan, A., Cui, Z., Xin, S., Xue, L., Xu, H., Park, K., and Goodenough, J.B. (2018). Garnet electrolyte with an ultralow interfacial resistance for Li-metal batteries. J. Am. Chem. Soc. *140*, 6448–6455.

79. Song, Y., Yang, L., Zhao, W., Wang, Z., Zhao, Y., Wang, Z., Zhao, Q., Liu, H., and Pan, F. (2019). Revealing the short-circuiting mechanism of garnet-based solid-state electrolyte. Adv. Energy Mater. *9*, 1900671.

80. Kumar, P.J., Nishimura, K., Senna, M., Düvel, A., Heitjans, P., Kawaguchi, T., Sakamoto, N., Wakiya, N., and Suzuki, H. (2016). A novel low-temperature solid-state route for nanostructured cubic garnet $Li_7La_3Zr_2O_{12}$ and its application to Li-ion battery. RSC Adv. *6*, 62656–62667.

81. Sakuda, A., Hayashi, A., and Tatsumisago, M. (2013). Sulfide solid electrolyte with favorable mechanical property for all-solid-state lithium battery. Sci. Rep. *3*, 2261.

82. Suzuki, Y., Kami, K., Watanabe, K., Watanabe, A., Saito, N., Ohnishi, T., Takada, K., Sudo, R., and Imanishi, N. (2015). Transparent cubic garnet-type solid electrolyte of Al_2O_3-doped $Li_7La_3Zr_2O_{12}$. Solid State Ionics *278*, 172–176.

83. David, I.N., Thompson, T., Wolfenstine, J., Allen, J.L., and Sakamoto, J. (2015).

Microstructure and Li-ion conductivity of hot-pressed cubic $Li_7La_3Zr_2O_{12}$. J. Am. Ceram. Soc. *98*, 1209–1214.

84. Garcia-Mendez, R., Mizuno, F., Zhang, R., Arthur, T.S., and Sakamoto, J. (2017). Effect of processing conditions of $75Li_2S$-$25P_2S_5$ solid electrolyte on its DC electrochemical behavior. Electrochim. Acta *237*, 144–151.

85. Zhang, Z., Zhang, L., Yan, X., Wang, H., Liu, Y., Yu, C., Cao, X., van Eijck, L., and Wen, B. (2019). All-in-one improvement toward Li_6PS_5Br-based solid electrolytes triggered by compositional tune. J. Power Sources *410-411*, 162–170.

86. Chung, H., and Kang, B. (2017). Mechanical and thermal failure induced by contact between a $Li_{1.5}Al_{0.5}Ge_{1.5}(PO_4)_3$ solid electrolyte and Li metal in an all solid-state Li cell. Chem. Mater. *29*, 8611–8619.

87. Duan, J., Wu, W., Nolan, A.M., Wang, T., Wen, J., Hu, C., Mo, Y., Luo, W., and Huang, Y. (2019). Lithium-graphite paste: an interface compatible anode for solid-state batteries. Adv. Mater. *31*, 1807243.

88. Chi, S.-S., Liu, Y., Zhao, N., Guo, X., Nan, C.-W., and Fan, L.-Z. (2019). Solid polymer electrolyte soft interface layer with 3D lithium anode for all-solid-state lithium batteries. Energy Storage Mater *17*, 309–316.

89. Liu, Y., Lin, D., Jin, Y., Liu, K., Tao, X., Zhang, Q., Zhang, X., and Cui, Y. (2017). Transforming from planar to three-dimensional lithium with flowable interphase for solid lithium metal batteries. Sci. Adv. *3*, eaao0713.

90. Shim, J., Lee, J.W., Bae, K.Y., Kim, H.J., Yoon, W.Y., and Lee, J.-C. (2017). Dendrite suppression by synergistic combination of solid polymer electrolyte crosslinked with natural terpenes and lithium-powder anode for lithium-metal batteries. ChemSusChem *10*, 2274–2283.

91. Cao, D., Zhang, Q., Hafez, A.M., Jiao, Y., Ma, Y., Li, H., Cheng, Z., Niu, C., and Zhu, H. (2019). Lignin-derived holey, layered, and thermally conductive 3D scaffold for lithium dendrite suppression. Small Methods *3*, 1800539.

92. Cao, D., Xing, Y., Tantratian, K., Wang, X., Ma, Y., Mukhopadhyay, A., Cheng, Z., Zhang, Q., Jiao, Y., Chen, L., and Zhu, H. (2019). 3D printed high-performance lithium metal microbatteries enabled by nanocellulose. Adv. Mater. *31*, 1807313.

93. Hafez, A.M., Jiao, Y., Shi, J., Ma, Y., Cao, D., Liu, Y., and Zhu, H. (2018). Stable metal anode enabled by porous lithium foam with superior ion accessibility. Adv. Mater. *30*, 1802156.

94. Cheng, X.-B., Yan, C., Zhang, X.-Q., Liu, H., and Zhang, Q. (2018). Electronic and ionic channels in working interfaces of lithium metal anodes. ACS Energy Lett. *3*, 1564–1570.

95. Guo, W., Liu, S., Guan, X., Zhang, X., Liu, X., and Luo, J. (2019). Mixed ion and electron-conducting scaffolds for high-rate lithium metal anodes. Adv. Energy Mater. *9*, 1900193.

96. Yan, C., Cheng, X.-B., Yao, Y.-X., Shen, X., Li, B.-Q., Li, W.-J., Zhang, R., Huang, J.-Q., Li, H., and Zhang, Q. (2018). An armored mixed conductor interphase on a dendrite-free lithium-metal anode. Adv. Mater. *30*, 1804461.

97. Yan, J., Yu, J., and Ding, B. (2018). Mixed ionic and electronic conductor for Li-metal anode protection. Adv. Mater. *30*, 1705105.

98. Wu, B., Wang, S., Lochala, J., Desrochers, D., Liu, B., Zhang, W., Yang, J., and Xiao, J. (2018). The role of the solid electrolyte interphase layer in preventing Li dendrite growth in solid-state batteries. Energy Environ. Sci. *11*, 1803–1810.

99. Lewis, J.A., Cortes, F.J.Q., Boebinger, M.G., Tippens, J., Marchese, T.S., Kondekar, N., Liu, X., Chi, M., and McDowell, M.T. (2019). Interphase morphology between a solid-state electrolyte and lithium controls cell failure. ACS Energy Lett. *4*, 591–599.

100. Zhang, X., Wang, S., Xue, C., Xin, C., Lin, Y., Shen, Y., Li, L., and Nan, C.-W. (2019). Self-suppression of lithium dendrite in all-solid-state lithium metal batteries with poly(vinylidene difluoride)-based solid electrolytes. Adv. Mater. *31*, 1806082.

101. Li, Y., Zhou, W., Chen, X., Lu, X., Cui, Z., Xin, S., Xue, L., Jia, Q., and Goodenough, J.B. (2016). Mastering the interface for advanced all-solid-state lithium rechargeable batteries. Proc. Natl. Acad. Sci. U S A *113*, 13313–13317.

102. Eshetu, G.G., Judez, X., Li, C., Bondarchuk, O., Rodriguez-Martinez, L.M., Zhang, H., and Armand, M. (2017). Lithium azide as an electrolyte additive for all-solid-state lithium–sulfur batteries. Angew. Chem. Int. Ed. *56*, 15368–15372.

103. Han, F., Yue, J., Zhu, X., and Wang, C. (2018). Suppressing Li dendrite formation in Li_2S-P_2S_5 solid electrolyte by LiI incorporation. Adv. Energy Mater. *8*, 1703644.

104. Tian, Y., Ding, F., Zhong, H., Liu, C., He, Y.-B., Liu, J., Liu, X., and Xu, Q. (2018). $Li_{6.75}La_3Zr_{1.75}Ta_{0.25}O_{12}$@amorphous Li_3OCl composite electrolyte for solid state lithium-metal batteries. Energy Storage Mater. *14*, 49–57.

105. Xu, R., Han, F., Ji, X., Fan, X., Tu, J., and Wang, C. (2018). Interface engineering of sulfide electrolytes for all-solid-state lithium batteries. Nano Energy *53*, 958–966.

106. Ahmad, Z., Xie, T., Maheshwari, C., Grossman, J.C., and Viswanathan, V. (2018). Machine learning enabled computational screening of inorganic solid electrolytes for suppression of dendrite formation in lithium metal anodes. ACS Cent. Sci. *4*, 996–1006.

107. Fitzhugh, W., Wu, F., Ye, L., Deng, W., Qi, P., and Li, X. (2019). A high-throughput search for functionally stable interfaces in sulfide solid-state lithium ion conductors. Adv. Energy Mater. *9*, 1900807.

108. Gao, Y., Wang, D., Li, Y.C., Yu, Z., Mallouk, T.E., and Wang, D. (2018). Salt-based organic–inorganic nanocomposites: towards a stable lithium metal/$Li_{10}GeP_2S_{12}$ solid electrolyte interface. Angew. Chem. Int. Ed. *57*, 13608–13612.

109. Han, X., Gong, Y., Fu, K., He, X., Hitz, G.T., Dai, J., Pearse, A., Liu, B., Wang, H., Rubloff, G., et al. (2016). Negating interfacial impedance in garnet-based solid-state Li metal batteries. Nat. Mater. *16*, 572.

110. Zhou, W., Zhu, Y., Grundish, N., Sen, X., Wang, S., You, Y., Wu, N., Gao, J., Cui, Z., Li, Y., and Goodenough, J.B. (2018). Polymer lithium-garnet interphase for an all-solid-state rechargeable battery. Nano Energy *53*, 926–931.

111. Zhang, Z., Zhang, L., Liu, Y., Wang, H., Yu, C., Zeng, H., Wang, L.-m., and Xu, B. (2018). Interface-engineered $Li_7La_3Zr2O_{12}$-based garnet solid electrolytes with suppressed Li-dendrite formation and enhanced electrochemical performance. ChemSusChem *11*, 3774–3782.

112. Hou, G., Ma, X., Sun, Q., Ai, Q., Xu, X., Chen, L., Li, D., Chen, J., Zhong, H., Li, Y., et al. (2018). Lithium dendrite suppression and enhanced interfacial compatibility enabled by an ex situ SEI on Li anode for LAGP-based all-solid-state batteries. ACS Appl. Mater. Interfaces *10*, 18610–18618.

113. Wang, C., Zhao, Y., Sun, Q., Li, X., Liu, Y., Liang, J., Li, X., Lin, X., Li, R., Adair, K.R., et al. (2018). Stabilizing interface between $Li_{10}SnP_2S_{12}$ and Li metal by molecular layer deposition. Nano Energy *53*, 168–174.

114. Wang, L., Zhang, L., Wang, Q., Li, W., Wu, B., Jia, W., Wang, Y., Li, J., and Li, H. (2018). Long lifespan lithium metal anodes enabled by Al_2O_3 sputter coating. Energy Storage Mater. *10*, 16–23.

115. Zhong, H., Sang, L., Ding, F., Song, J., and Mai, Y. (2018). Conformation of lithium-aluminium alloy interphase-layer on lithium metal anode used for solid state batteries. Electrochim. Acta *277*, 268–275.

116. Fu, K., Gong, Y., Liu, B., Zhu, Y., Xu, S., Yao, Y., Luo, W., Wang, C., Lacey, S.D., Dai, J., et al. (2017). Toward garnet electrolyte–based Li metal batteries: an ultrathin, highly effective, artificial solid-state electrolyte/metallic Li interface. Sci. Adv. *3*, e1601659.

117. Luo, W., Gong, Y., Zhu, Y., Fu, K.K., Dai, J., Lacey, S.D., Wang, C., Liu, B., Han, X., Mo, Y., et al. (2016). Transition from superlithiophobicity to superlithiophilicity of garnet solid-state electrolyte. J. Am. Chem. Soc. *138*, 12258–12262.

118. Luo, W., Gong, Y., Zhu, Y., Li, Y., Yao, Y., Zhang, Y., Fu, K., Pastel, G., Lin, C.-F., Mo, Y., et al. (2017). Reducing interfacial resistance between garnet-structured solid-state electrolyte and Li-metal anode by a germanium layer. Adv. Mater. *29*, 1606042.

119. Xu, H., Li, Y., Zhou, A., Wu, N., Xin, S., Li, Z., and Goodenough, J.B. (2018). Li3N-Modified garnet electrolyte for all-solid-state lithium metal batteries operated at 40°C. Nano Lett. *18*, 7414–7418.

120. Wang, C., Yang, Y., Liu, X., Zhong, H., Xu, H., Xu, Z., Shao, H., and Ding, F. (2017). Suppression of lithium dendrite formation by using LAGP-PEO (LiTFSI) composite solid electrolyte and lithium metal anode modified by PEO (LiTFSI) in all-solid-state lithium batteries. ACS Appl. Mater. Interfaces *9*, 13694–13702.

121. Ma, Q., Zeng, X.-X., Yue, J., Yin, Y.-X., Zuo, T.-T., Liang, J.-Y., Deng, Q., Wu,

X.-W., and Guo, Y.-G. (2019). Viscoelastic and nonflammable interface design–enabled dendrite-free and safe solid lithium metal batteries. Adv. Energy Mater. *9*, 1803854.

122. Zhang, W., Weber, D.A., Weigand, H., Arlt, T., Manke, I., Schröder, D., Koerver, R., Leichtweiss, T., Hartmann, P., Zeier, W.G., and Janek, J. (2017). Interfacial processes and influence of composite cathode microstructure controlling the performance of all-solid-state lithium batteries. ACS Appl. Mater. Interfaces *9*, 17835–17845.

123. Motoyama, M., Ejiri, M., and Iriyama, Y. (2015). Modeling the nucleation and growth of Li at metal current collector/LiPON interfaces. J. Electrochem. Soc. *162*, A7067–A7071.

124. Westover, A.S., Dudney, N.J., Sacci, R.L., and Kalnaus, S. (2019). Deposition and confinement of Li metal along an artificial lipon-lipon interface. ACS Energy Lett. *4*, 651–655.

125. Wang, C., Gong, Y., Dai, J., Zhang, L., Xie, H., Pastel, G., Liu, B., Wachsman, E., Wang, H., and Hu, L. (2017). In situ neutron depth profiling of lithium metal-garnet interfaces for solid state batteries. J. Am. Chem. Soc. *139*, 14257–14264.

126. Seitzman, N., Guthrey, H., Sulas, D.B., Platt, H.A.S., Al-Jassim, M., and Pylypenko, S. (2018). Toward all-solid-state lithium batteries: three-dimensional visualization of lithium migration in β-Li_3PS_4 ceramic electrolyte. J. Electrochem. Soc. *165*, A3732–A3737.

127. Zheng, J., Tang, M., and Hu, Y.-Y. (2016). Lithium ion pathway within $Li_7La_3Zr_2O_{12}$-polyethylene oxide composite electrolytes. Angew. Chem. Int. Ed. *55*, 12538–12542.